Multi-mode spin wave system excited by pure spin current

MSc thesis

Philipp Seibt, WWU Münster
Student no. 362204

Supervisors
Prof. Dr. Sergej O. Demokritov
Dr. Vladislav E. Demidov

Münster, May 2015

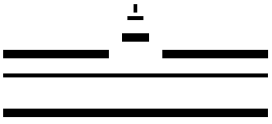

Westfälische
Wilhelms-Universität
Münster

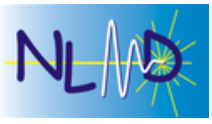

Abstract

In magnonics the key idea is to use spin waves for information processing. The excitation of spin waves using pure spin currents induced by the spin Hall effect shows great prospects for the design of power efficient, fully planar magnonic devices. By means of experimental microfocus Brillouin light scattering spectroscopy and numerical micromagnetic simulation we have investigated the effect of a pure spin current on a multi-mode spin wave system. Contrary to theoretical predictions we find that several modes can be excited simultaneously. Although the spin current is spatially uniform we observe that it affects spin waves in a spatially non-uniform way. Using these results we demonstrate the power efficient excitation of a spin wave mode and the mode selective excitation of one single mode using a pure spin current.

Contents

1 Introduction

Magnetic nanostructures have attracted a lot of interest of researchers and engineers alike when magnetic hard disks found their way into every day computers during the last decades [1]. The discovery of the giant magnetoresistance (GMR) effect by Grünberg and Fert once more boosted storage capacities and was rewarded with the Nobel prize in 2007 [2, 3]. It was also the starting point for spintronics [4, 5]. In spintronics not only the charge of an electron is used as a carrier of information, but also the spin.

In recent years researchers have been working on the idea of magnonics to go one step further [6–9]. In magnonics, spin waves or their quasiparticle analogon magnons are used for information processing. In general, magnonics deals with the excitation, manipulation and detection of spin waves.

Spin waves were introduced by Bloch in 1930 to explain the temperature dependence of the static magnetization of ferromagnets at low temperature [10]. A spin wave is the precession of magnetic moments in a magnetic material with a coherent phase relation [7]. Spin waves can be excited using rf magnetic fields [11], ultrashort laser pulses [12] or spin-polarized electric currents [13–15]. In the latter, an electric current typically flows through a trilayer made up of a non-magnetic layer sandwiched between two ferromagnetic layers. The current is spin-polarized in the first magnetic layer, which can destabilize the magnetization in the second layer. The term spin-torque nanooscillator has been coined for these structures [16].

Recently it was discovered that magnetization dynamics can also be excited by pure spin currents without an electric current flowing in the magnetic structure at all [17–20]. This allows for the design of fully planar devices. The devices are also expected to be less affected by heating due to the current. The experiments in many cases utilize the spin Hall effect in non-magnetic materials with large spin-orbit coupling [21,22]. It has been shown that pure spin currents can excite ferromagnetic resonance (FMR) [19, 23], reversibly switch the magnetization [18], modify the damping of a magnetic system [17, 24–26] and control parametric excitation of spin waves [27]. Fundamental modes in confined structures were also investigated [23, 28]. Above a threshold coherent auto-oscillations can also be excited, if the spin current is spatially non-uniform [20, 29–35]. These systems are referred to as spin Hall nanooscillators.

However, those samples were treated as single-mode systems where only one spin wave mode exists. It is well known, however, that the confinement of magnetic structures leads to a rich mode structure due to an inhomogeneous internal mag-

netic field [36]. Such multi-mode systems have great potential for technical applications [37]. Theory for spin-torque induced magnetization dynamics predicts that only one single spin wave mode should be stable in the steady state regime and the simultaneous excitation of two modes is impossible in most situations [38, 39]. The reason for this is that the two modes compete for the same energy source, namely the spin current. Most experiments in spin-torque nanooscillators and spin Hall nanooscillators have confirmed this prediction (see [38] for a review). In some experiments mode hopping was observed in the steady state, that means the system switched between two oscillation states on a sub-nanosecond time scale [40, 41]. The coupling of two modes was also reported [42]. To investigate a system that supports more than one spin wave mode can therefore be considered to be of interest for both fundamental physics as well as technical applications.

In this thesis we report the investigation of a multi-mode spin wave system excited by pure spin current. We have studied the magnetization dynamics in an equilateral Permalloy ($Ni_{80}Fe_{20}$) triangle both experimentally and by means of micromagnetic simulations. First, we discuss the basic equation of motion for a ferromagnet under the influence of damping and a pure spin current in Chapter 2. In Chapter 3 we give details on the experimental technique and sample as well as the simulation framework and the micromagnetic models under investigation. In Chapter 4 the results are presented. We discuss the experimental findings and develop the micromagnetic model, gradually approaching the experimental situation. In Chapter 5 we review experiment and simulation and point out possibilities for future research.

2 Theoretical considerations

In this Chapter the theoretical tools needed to analyse the magnetization dynamics at hand are presented. The aim is rather to summarize the main ideas behind these tools than to provide a rigorous derivation. First, the magnetization dynamics in thin films is discussed. Then, Gilbert damping is introduced and, finally, the influence of a spin current is included.

In general, the magnetization dynamics in a ferromagnet under the influence of damping and a spin current can be described by the Landau-Lifshitz-Gilbert-Slonczewski equation:

$$\frac{\partial \vec{M}}{\partial t} = \vec{\tau_{\mathrm{H}}} + \vec{\tau_{\mathrm{G}}} + \vec{\tau_{\mathrm{S}}}, \tag{2.1}$$

where $\vec{\tau_{\mathrm{H}}}$ describes the conservative motion, $\vec{\tau_{\mathrm{G}}}$ describes damping on a phenomenological basis and $\vec{\tau_{\mathrm{S}}}$ describes the action of the spin current [38].

2.1 Conservative motion

2.1.1 Equation of motion and energy contributions

Let us rationalize the conservative part $\vec{\tau_{\mathrm{H}}}$ of the above differential equation. In classical mechanics the evolution of the angular momentum $\vec{L}$ of a body is given by

$$\frac{d\vec{L}}{dt} = \vec{\tau}, \tag{2.2}$$

where $\vec{\tau}$ is the torque acting on the body. On the other hand, the torque acting on a magnetic moment $\vec{m}$ in a magnetic field $\vec{H}$ reads [43, p. 84]

$$\vec{\tau} = \vec{m} \times \vec{H}. \tag{2.3}$$

The magnetic moment and the angular momentum are connected by the relation $\vec{m} = -\gamma \vec{L}$, so that [43, p. 85]

$$\frac{d\vec{m}}{dt} = -\gamma \vec{m} \times \vec{H}. \tag{2.4}$$

The gyromagnetic ratio γ for an electron is given by

$$\gamma = \frac{eg\mu_0}{2m_\mathrm{e}}, \tag{2.5}$$

where $e > 0$ is the modulus of the electron charge, g is the g-factor, μ_0 is the vacuum permeability and m_e is the electron mass. In the framework we are going to use we can regard γ as a material constant.

To describe the dynamics of a ferromagnetic sample instead of a single magnetic moment we introduce the continuous, macroscopic magnetization $\vec{M} = \vec{M}(\vec{r}, t)$ by summing over all magnetic moments in the sample [44, p. 9]:

$$\vec{M} = \frac{\sum_i \vec{m}_i}{V}, \tag{2.6}$$

where $\vec{m}_i$ are the magnetic moments in the volume V. In general, these magnetic moments comprise contributions from the spin as well as the orbital angular momentum of electrons and, hereby, incorporate the atomic structure of the ferromagnetic sample [44, p. 3]. If all magnetic moments within a sample are aligned the magnetization reaches its maximum value, the so called saturation magnetization M_S. With the definition (2.6) we get the differential equation for the dynamics of the magnetization using Equation (2.4):

$$\frac{\partial \vec{M}}{\partial t} = -\gamma \vec{M} \times \vec{H}. \tag{2.7}$$

In the case of a static magnetic field $\vec{H}$ this equation of motion describes the right-hand precession of the magnetization $\vec{M}$ about $\vec{H}$ with the Larmor frequency $\omega = \gamma H$ [43, p. 85]. For many magnetic materials, including Permalloy used in this thesis, $\gamma \approx 2.8\,\mathrm{MHz/Oe}$. Hence, for fields between 10 Oe and 1000 Oe, which can easily be achieved experimentally, the frequency of precession lies between 28 MHz and 2.8 GHz. The fact that the frequency can be continuously tuned by the magnetic field remains valid for more complex systems and is a central advantage of magnonics [8].

By introducing an effective magnetic field $\vec{H}_\mathrm{eff}$ not only static external fields but many other influences on the magnetization dynamics can be included into Equation (2.7). The field can be derived from the free energy volume density $\mathcal{W}$ [44, pp. 32]:

$$\vec{H}_\mathrm{eff} = -\frac{\delta \mathcal{W}}{\delta \vec{M}}. \tag{2.8}$$

Here, δ denotes to the variational derivative. In situations relevant for this thesis $\mathcal{W}$ has four important contributions [45]:

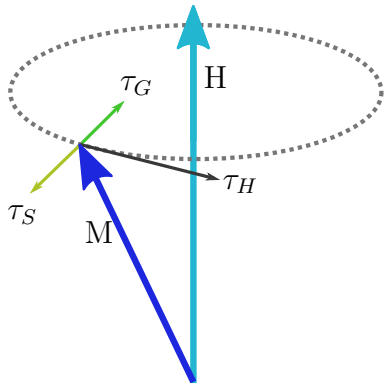

Figure 2.1: Torques influencing the magnetization M in the framework of the Landau-Lifshitz-Gilbert-Slonczewski equation. τ_H is caused by the effective magnetic field, τ_G by damping and τ_S by a spin polarized current. For the assumptions underlying the picture see text.

- **Zeeman energy:** This term describes the interaction of the magnetization with an external field $\vec{H}$. It is given by: $\mathcal{W}_Z = -\vec{M}\vec{H}$. The Zeeman energy is minimal for an alignment of the magnetization with the field.

- **Demagnetizing energy:** This term arises due to the finite lateral dimensions of magnetic samples. At the surfaces fictitious magnetic charges appear, because they cannot be compensated by neighbouring magnetic moments. These charges are the origin of the demagnetizing field $\vec{H}_\mathrm{demag}$ within the sample and the stray field outside of the sample [43, pp. 49]. The demagnetizing field is always directed opposite to the magnetization. It depends on the sample shape and can be inhomogeneous in space. Often, the external and the demagnetizing field are combined to give the internal field: $\vec{H}_\mathrm{int} = \vec{H} + \vec{H}_\mathrm{demag}$. The internal field plays an important role in defining the frequency and spatial profile of spin waves in confined structures.

- **Exchange energy:** The exchange energy has its origin in the quantum mechanical Pauli exclusion principle and was first described by Heisenberg [46]. It favours an alignment of neighbouring spins. The strength of the exchange energy is characterised by the exchange constant A, which can again be regarded as a material parameter. The exchange energy becomes important for spin waves when the wavelength λ is of the order of the exchange length $l_\mathrm{ex} = \sqrt{\frac{A}{2\pi M_\mathrm{S}^2}}$ [47]. The exchange length in Permalloy is $l_\mathrm{ex} \approx 6\,\mathrm{nm}$.

- **Anisotropy energy:** This term describes the fact that many ferromagnets can be magnetized in one direction more easily than in another [48, pp. 83]. The most common anisotropy is magnetocrystalline anisotropy originating in the crystal structure of the magnet. In Permalloy, magnetocrystalline anisotropy is negligible.

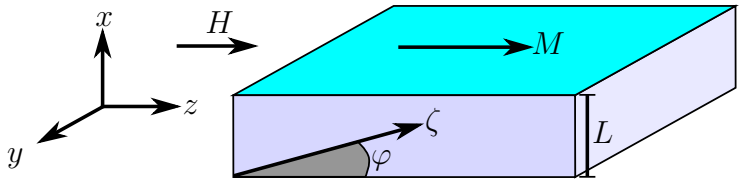

Figure 2.2: Coordinate system used for the infinite thin film dispersion relation. An infinite film with thickness L and magnetization M is shown. Plane waves travel along ζ enclosing an angle φ with the z-axis.

With the effective field we finally get the conservative part of the Landau-Lifshitz-Gilbert-Slonczewski equation (2.1):

$$\vec{\tau}_{\mathrm{H}} = -\gamma \vec{M} \times \vec{H}_{\mathrm{eff}}. \tag{2.9}$$

We see that $\vec{\tau}_{\mathrm{H}}$ stands perpendicular on both the magnetization and the effective field. This situation is depicted in Figure 2.1 assuming that the equilibrium direction of the magnetization coincides with the field. In this picture $\vec{M}$ precesses about the field $\vec{H}$.

2.1.2 Spin waves in thin films

The Landau-Lifshitz equation $\partial \vec{M}/\partial t = \vec{\tau}_{\mathrm{H}}$ has been analysed for numerous geometries and taking into account different energy contributions. An overview is given in [44]. Of particular importance for applications is the analysis of spin waves in an in-plane magnetized, thin film [43, p. 52]. Such a film is sketched in Figure 2.2.

Kittel derived the frequency for the uniform magnetization precession, i.e. the wave vector $k = 0$, in such a film [49]. The corresponding Kittel formula is given by

$$\omega_0 = \gamma \sqrt{H(H + 4\pi M_{\mathrm{S}})}. \tag{2.10}$$

Damon and Eshbach extended the analysis to spin waves with $k > 0$, however, still neglecting the exchange energy [50]. To include this energy contribution and calculate the full spin wave spectrum is mathematically demanding [51–53]. Here, we focus on the relevant results for this thesis. We mainly follow [51].

Consider a ferromagnetic film with thickness L in the x-direction and unbound in y- and z-direction (Figure 2.2). The film is magnetized to saturation by an external field H in z-direction. In the calculations the Landau-Lifshitz equation is linearised and the magnetostatic approximation of the Maxwell equations and exchange boundary conditions [54] are taken into account. The spin wave is assumed to be a plane wave along the ζ-direction enclosing an angle φ with the z-axis:

$$\vec{m}(\zeta, t) \propto \exp\left[\mathrm{i}(\omega t - k_\zeta \zeta)\right]. \tag{2.11}$$

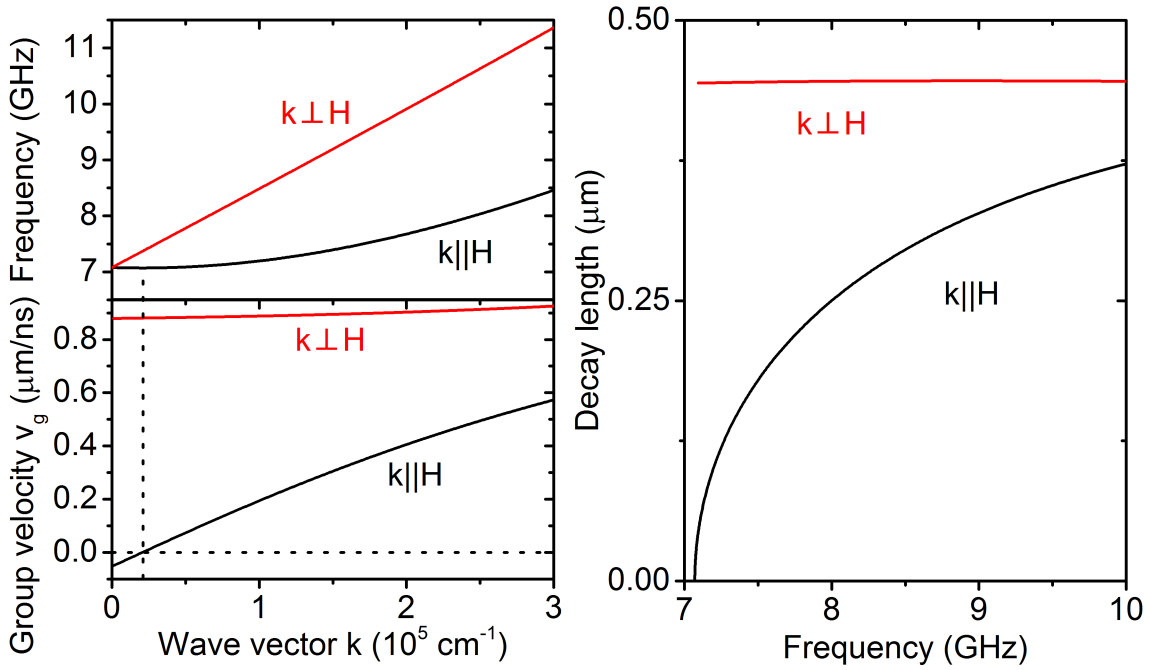

Figure 2.3: Spin wave dispersion for a thin film. Spin wave frequency and group velocity as a function of wave vector k as well as decay length as a function of frequency for spin waves travelling parallel to the magnetic field, $k||H$, and perpendicular to it, $k\perp H$, in a thin film. Parameters: $\gamma = 2.8\,\mathrm{MHz/Oe}$, $A = 1.3 \times 10^{-6}\,\mathrm{erg/cm}$, $4\pi M_\mathrm{S} = 10053\,\mathrm{G}$, $H = 600\,\mathrm{Oe}$, $L = 5\,\mathrm{nm}$, $\alpha_\mathrm{G} = 0.02$.

Then, for the case that the distribution of the dynamic magnetization across the film thickness is uniform, an approximate dispersion relation can be derived:

$$\omega^2(k) = \Big[\omega_\mathrm{H} + \omega_\mathrm{M}\big(1 + l_\mathrm{ex}^2 k^2 - P\big)\Big]\Big[\omega_\mathrm{H} + \omega_\mathrm{M}\big(l_\mathrm{ex}^2 k^2 + P\sin^2(\varphi)\big)\Big]$$
$$\text{with } \omega_\mathrm{H} = \gamma H,\ \omega_\mathrm{M} = \gamma 4\pi M_\mathrm{S} \text{ and } P = 1 - \frac{1}{kL}\big(1 - \exp(-kL)\big). \tag{2.12}$$

Figure 2.3 shows the dispersion relation for a Permalloy film with a thickness $L = 5\,\mathrm{nm}$ and $H = 600\,\mathrm{Oe}$ for the cases $k||H$ ($\varphi = 0°$) and $k\perp H$ ($\varphi = 90°$). Below, the group velocity

$$v_\mathrm{g}(\varphi = \overline{\varphi}) = \frac{\partial\omega(\varphi = \overline{\varphi})}{\partial k} \tag{2.13}$$

is shown. We outline the characteristic features of the dispersion:

- The frequency lies in the GHz range, the group velocity is of the order of $1\,\mu\mathrm{m/ns}$.

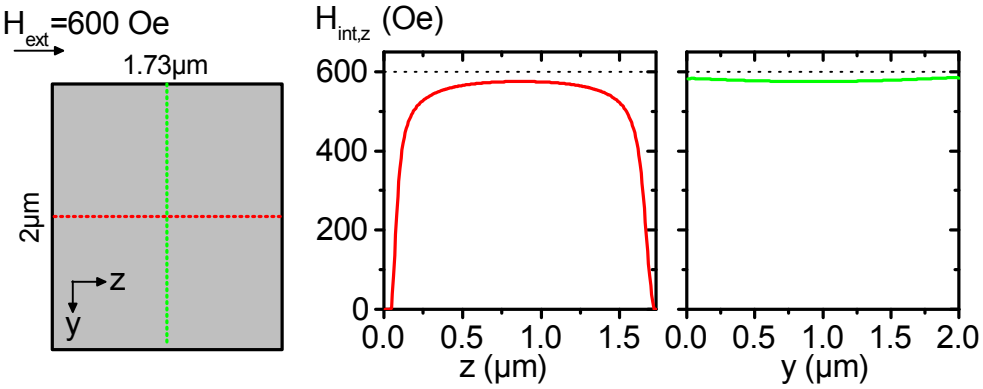

Figure 2.4: Internal field in a Permalloy rectangle. z-component of the internal field in a 10 nm×2000 nm×1730 nm Py rectangle subject to an external field along z with $H_{\text{ext}} = 600$ Oe. Field was calculated with MuMax3.

- Both branches meet at $k = 0$ at the cutoff frequency $f_0 = \omega_0/2\pi \approx 7.1$ GHz. Waves with a frequency lower than f_0 are exponentially damped in the film.
- For $k||H$ the group velocity is negative until $k \approx 0.2 \times 10^5\,\text{cm}^{-1}$. This is why these waves are called backward volume waves [55, pp. 158]. The minimum of the dispersion is much more pronounced in thicker films. However, for $L = 5$ nm nearly the whole spectrum is dominated by the exchange energy and the frequency rises roughly quadratically with increasing k.
- For $k\perp H$ the group velocity is always positive and higher compared to $k||H$. In thick films these waves are located at the surface of the film and their dynamic amplitude decreases exponentially away from the surface, so they are referred to as surface waves [55, pp. 162].

2.1.3 Spin wave confinement

The lateral confinement of spin waves in all three dimensions has two main consequences: The internal field H_{int} becomes strongly inhomogeneous and the wave vector of the modes become quantized.

Inhomogeneous internal field

The confinement of spin waves leads to additional magnetic charges at the surfaces. In magnetic elements where the thickness is much smaller compared to the lateral dimensions this leads to an inhomogeneous demagnetizing field and consequently to an inhomogeneous internal field [56]. As an example the internal field in a Py rectangle subjected to an external field of $H_{\text{ext}} = 600$ Oe along the z-direction is shown in Figure 2.4. The plot is the result of a micromagnetic simulation (see Chapter 3). We see that the internal field is nearly constant in the center of the

rectangle. There it has a value of $H_{\text{int}} \approx 580\,\text{Oe}$. However, at the edges along the z-direction a strong decrease is observed until the field is zero.

This decrease leads to the appearance of a new class of modes: so called edge or localized modes [57–60]. They get their name from the fact that they are localized at the edges of a sample. We can rationalize this by assuming local validity of the dispersion relation (2.12) [59]. However, instead of the external field now the internal field enters the expression. At the edges this field is lower, hence, the frequency of edge modes is lower compared to usual modes in a thin film. Also, these modes cannot extend into the center of the film, because they are exponentially damped due to their low frequency.

In the center of the sample the consequences of the inhomogeneous magnetic field are less severe. As the internal field is lowered by 20 Oe compared to the infinite film case the frequencies in the center will be lower as well.

Quantized wave vector

If spin waves in a magnetic element can propagate from end to end of the sample it becomes a magnetic resonator [61]. Then, only standing spin waves can exist. Due to the lack of propagation the rigorous definition of a wave vector is difficult. However, one can still introduce a characteristic wave vector which will be quantized. In a simple quantization scheme a sinusoidal dependence of the dynamic magnetization is assumed [59]. If the spin wave is localized in an area with side lengths of l_z and l_y in z- and y-direction, respectively, the corresponding characteristic wave vectors are given by

$$k_z = \frac{(n+1)\pi}{l_z} \text{ and } k_y = \frac{(m+1)\pi}{l_y}, \tag{2.14}$$

with $m, n = 0, 1, ...$ Here, $l_{y,z}$ are called localization lengths. The dispersion relation (2.12) can then still be used as a good approximation with $k = \sqrt{k_y^2 + k_z^2}$ and $\varphi = \arctan\left(\frac{k_y}{k_z}\right)$.

2.2 Damping

The Landau-Lifshitz equation describes the conservative motion of the magnetization - if the effective field is constant, the magnetization precession goes on forever. This is in contradiction to physical reality, where damping leads to a decrease of the precession angle. In 1955 Gilbert developed a theory that allows for the phenomenological description of damping [45]. This model was generalized by Slavin and Tiberkevich in 2007 to account for a precession with larger precession angles [62]. These models do not contain any information about the physical origins of the damping, which in general are magnon-magnon interactions, energy transfer to phonons or to the conduction electrons [45].

In the phenomenological approach a torque $\vec{\tau}_\mathrm{G}$ is added to the Landau-Lifshitz equation [62]:

$$\frac{\partial \vec{M}}{\partial t} = \vec{\tau}_\mathrm{H} + \vec{\tau}_\mathrm{G} \tag{2.15}$$

$$\text{with } \vec{\tau}_\mathrm{G} = \frac{\alpha(\xi)}{M_\mathrm{S}} \left(\vec{M} \times \frac{\partial \vec{M}}{\partial t} \right). \tag{2.16}$$

Here, ξ is given by

$$\xi = \frac{(\partial \vec{M}/\partial t)^2}{\omega_\mathrm{M}^2 M_\mathrm{S}^2}. \tag{2.17}$$

For finite precession angles the expression for α can be expanded into a Taylor series

$$\alpha(\xi) = \alpha_\mathrm{G}(1 + q_1\xi + q_2\xi^2 + ...), \tag{2.18}$$

with $q_i \approx 1$. If only the zeroth order is considered the traditional Gilbert damping torque is recovered:

$$\vec{\tau}_\mathrm{G} = \frac{\alpha_\mathrm{G}}{M_\mathrm{S}} \left(\vec{M} \times \frac{\partial \vec{M}}{\partial t} \right). \tag{2.19}$$

Here, the dimensionless α_G is called Gilbert damping parameter and typically $\alpha_\mathrm{G} \ll 1$ holds. In the case of Permalloy on Pt $\alpha_\mathrm{G} \approx 0.02$. The Gilbert torque is depicted in Figure 2.1. It stands perpendicular on the field $\vec{H}$, the magnetization $\vec{M}$ and the conservative torque $\vec{\tau}_\mathrm{H}$ and leads to a reduction of the precession angle.

If α_G is small, which is the case for all materials at interest in magnonics, damping can be included into the analysis in Section 2.1 by substituting $\omega_\mathrm{H} \to \omega_\mathrm{H} + i\alpha_\mathrm{G}\omega$ and the dispersion relation (2.12) can still be used [44, p. 19]. However, the frequency then becomes imaginary $\omega = \omega' + i\omega_\mathrm{r}$, where ω' is given by Equation (2.12) and the relaxation rate ω_r is given by [44, pp. 167]

$$\omega_\mathrm{r} = \alpha_\mathrm{G}\omega' \frac{\partial \omega'}{\partial \omega_\mathrm{H}}. \tag{2.20}$$

This means that in resonance experiments the linewidth of a spin wave resonance will be broadened due to damping [44, pp. 17].

On the other hand, one can also define an imaginary wave vector $k = k' + ik''$. k''^{-1} has the physical meaning of a decay length and is given by

$$k''^{-1} = \frac{v_\mathrm{g}}{\omega_\mathrm{r}}. \tag{2.21}$$

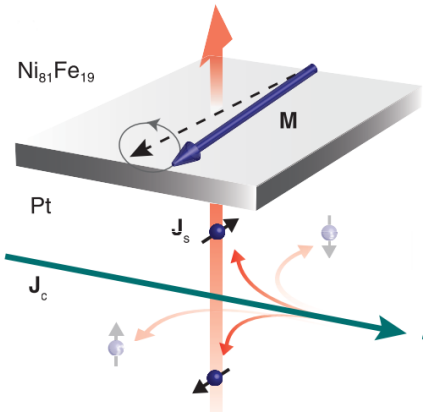

Figure 2.5: Cartoon showing the basics of the spin Hall effect. A charge current j_c flows through a Pt layer. Due to spin-orbit coupling spin is accumulated at the boundaries. This can be described as a spin current j_S that can interact with the magnetization M of e.g. Permalloy. Figure from [17].

In Figure 2.3 the decay length is shown as a function of spin wave frequency for the thin Permalloy film with $\alpha_G = 0.02$. One sees that the decay length is of the order of 1 µm in such a film.

2.3 Spin current

We give a short introduction into the spin Hall effect and describe how it can be included in the above analysis.

2.3.1 Spin Hall effect

The main idea of the spin Hall effect is that an unpolarized charge current $\vec{j}_c$ flowing through a conductor can be accompanied by a spin current $\vec{j}_s$ [22]. This was first discovered in semiconductors [63] and later extended to paramagnetic metals [21].

The situation is depicted in the cartoon in Figure 2.5 for the spin Hall effect in Pt. A charge current $\vec{j}_c$ flows through the layer. Scattering of the electrons at impurities [64] in combination with strong spin-orbit coupling results in a spin imbalance across the layer. This is analogous to a spin current perpendicular to the charge current, $\vec{j}_s \perp \vec{j}_c$. In general, this is a three dimensional problem, but in this thesis a spin current in only one direction is of importance.

The ratio of spin and charge current defines the efficiency of the spin current generation and is called spin Hall angle ϕ_H. For Pt the reported values of ϕ_H differ by one order of magnitude, probably due to different measurement techniques. We find $\phi_H = 0.01$ [65], $\phi_H = 0.11$ [66] and $\phi_H = 0.076$ [19] in the literature.

If a ferromagnet is brought into contact with the conductor the electrons scatter at the interface and hereby transfer angular momentum from the conducting to the

magnetic layer (or vice versa). This can be described in a phenomenological way by a spin transfer torque (STT) acting on the magnetization in the magnet [67]. Magnetization dynamics in that layer can then be excited or suppressed [28, 68].

2.3.2 Slonczewski torque

The idea of spin transfer was introduced by Slonczewski and Berger in 1996 [69–71]. However, they did not look at spin transfer induced by the spin Hall effect but rather at magnetic multilayer structures consisting of a "fixed" magnetic layer, a non-magnetic spacer and a "free" magnetic layer. Following [38], a charge current I gets spin-polarized in the fixed layer with an efficiency ε in the direction of the unit vector $\vec{e_p}$. This spin-polarized current then exerts a torque

$$\vec{\tau}_{\mathrm{S}} = \frac{\sigma_0 I(\vec{r})}{M_{\mathrm{S}}} \left[\vec{M} \times \left[\vec{M} \times \vec{e_p}\right]\right] \tag{2.22}$$

on the magnetization in the free layer. Here, σ_0 is given by

$$\sigma_0 = \frac{\varepsilon g \mu_B}{2e M_{\mathrm{S}} L S}, \tag{2.23}$$

where g is the spectroscopic Lande factor, μ_B is the Bohr magneton, e is the modulus of the electric charge, M_{S} is the saturation magnetization, L is the thickness of the free layer and S is the area of the current-carrying region, so that the charge current density is $j_c(\vec{r}) = I(\vec{r})/S$. The current can in principal be spatially inhomogeneous. However, if not marked otherwise, we will assume a spatially homogeneous current $I(\vec{r}) = I$ in this thesis.

The torque $\vec{\tau}_{\mathrm{S}}$ can also be used for STT induced by the spin Hall effect, because the above equations do not explicitly model the fixed layer, but only incorporate the characteristics of the spin-polarized current. By substituting the efficiency ε with the spin Hall angle ϕ_{H}, spin Hall effect induced dynamics can be considered.

Let us define

$$\vec{M} = \begin{pmatrix} m_x \\ m_y \\ M_{\mathrm{S}} \end{pmatrix}, \ \vec{H}_{\mathrm{eff}} = \begin{pmatrix} 0 \\ 0 \\ H \end{pmatrix}, \ \vec{e_p} = \begin{pmatrix} 0 \\ 0 \\ 1 \end{pmatrix}. \tag{2.24}$$

Then, for $m_x, m_y \ll M_{\mathrm{S}}$ and small α_{G} we can substitute in the damping torque $\vec{\tau}_{\mathrm{G}}$ the exact time derivative by the conservative torque $\vec{\tau}_{\mathrm{H}}$. This yields

$$\vec{\tau}_{\mathrm{G}} \approx \frac{\gamma \alpha_{\mathrm{G}}}{M_{\mathrm{S}}} \vec{M} \times \left[\vec{H}_{\mathrm{eff}} \times \vec{M}\right] = -\alpha_{\mathrm{G}} \omega_{\mathrm{H}} \begin{pmatrix} m_x \\ m_y \\ 0 \end{pmatrix} \text{ and } \vec{\tau}_{\mathrm{S}} = -\sigma_0 I \begin{pmatrix} m_x \\ m_y \\ 0 \end{pmatrix}. \tag{2.25}$$

We see that the damping torque and the spin transfer torque are collinear. Hence, the spin transfer torque can either enhance or suppress magnetization dynamics, depending on the sign of the current I. Therefore, the spin current is sometimes referred to as "negative damping". Figure 2.1 shows the different torques for a small angle precession of the magnetization. Note that in a film, in the above expression $\alpha_{\mathrm{G}}\omega_{\mathrm{H}}$ has to be replaced by ω_{r} (Equ. (2.20)) [72].

If the current I exceeds a threshold I_{th} enough $I > I_{\mathrm{th}}$, it can completely compensate the damping and enable auto-oscillation of the magnetization [20, 29, 31, 33, 34, 73–75].

In this thesis we are interested in the dynamics below the compensation point $I < I_{\mathrm{th}}$. Following [38], for the excitation of a single spin wave mode it is convenient to rewrite the Landau-Lifshitz-Gilbert-Slonczewski equation in terms of a complex spin wave amplitude

$$c = \frac{m_x - i m_y}{\sqrt{2M_{\mathrm{S}}(M_{\mathrm{S}} + m_z)}}, \tag{2.26}$$

where $\vec{M} = (m_x, m_y, m_z)$. We then get a differential equation

$$\underbrace{\frac{dc}{dt} + i\omega(p)\cdot c}_{\text{Conservative motion}} + \underbrace{\Gamma_+(p)\cdot c}_{\text{Gilbert damping}} - \underbrace{\Gamma_-(p)\cdot c}_{\text{Spin transfer torque}} = \underbrace{f(t)}_{\text{External force}}, \tag{2.27}$$

where $p = |c|^2$ is the power and $f(t)$ is some external driving force, e.g. a magnetic field or a thermal bath. The remaining expressions are only considered in the weakly-nonlinear regime ($p \ll 1$) and are given by

$$\omega(p) \approx \omega(p=0) + Np, \tag{2.28}$$
$$\Gamma_+(p) \approx \omega_{\mathrm{r}}(1 + Qp) \text{ and} \tag{2.29}$$
$$\Gamma_-(p) \approx \sigma_0 I(1-p). \tag{2.30}$$

Here, N characterises a possible non-linear frequency shift with increasing power and Q determines how the damping evolves with rising p. For an in-plane magnetized film Q incorporates the expansion of the damping coefficient α (Equ. (2.18)) up to first order, i.e. $\alpha(\xi) \approx \alpha_{\mathrm{G}}(1 + q_1\xi)$.

Without any external driving force, one can find the threshold current for auto-oscillation from Equation (2.27):

$$I_{\mathrm{th}} = \frac{\omega_{\mathrm{r}}}{\sigma_0}. \tag{2.31}$$

Physically this corresponds to the situation where the current *exactly* compensates the losses of the system.

If thermal fluctuations according to the fluctuation dissipation theorem [76] are

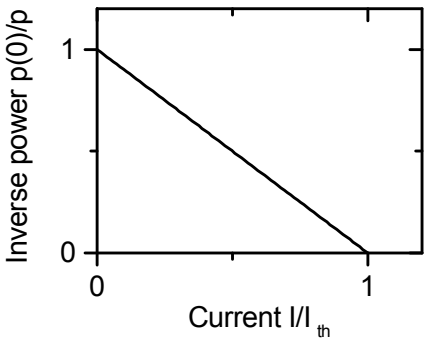

Figure 2.6: Inverse power as a function of current. Current dependence as predicted by Equ. (2.32).

considered as the external driving force, one can calculate the mean power $\overline{p}$. In this thesis, we will usually analyse the inverse power normalised at zero current instead. The theoretical expression for $I < I_{\mathrm{th}}$ is given by

$$\frac{\overline{p}(I=0)}{\overline{p}(I)} = 1 - \frac{\Gamma_-(p=0)}{\Gamma_+(p=0)} = 1 - \frac{\sigma_0 I}{\omega_{\mathrm{r}}}. \tag{2.32}$$

In this approximation we get a linear dependence of the inverse power on the current (Figure 2.6). The slope is given by

$$\frac{\sigma_0}{\omega_{\mathrm{r}}} = \frac{\varepsilon g \mu_B}{2eM_{\mathrm{S}}LS\omega_{\mathrm{r}}}. \tag{2.33}$$

As this expression relies on an expansion around $p = 0$ we expect it to fail for I in the proximity of I_{th}. Instead a more complicated expression is found for the whole range of bias currents, that is given by Equation (84) in [38].

3 Methods

Our study is motivated by experiments done with an equilateral triangle made of Permalloy. We describe the experimental technique used to obtain these results and the sample. Then we introduce micromagnetic simulation and present the models investigated in this thesis.

3.1 Experiments

3.1.1 Micro-Brillouin Light Scattering Spectroscopy

Microfocus Brillouin light scattering spectroscopy (microBLS) was used to investigate the magnetization dynamics in a Permalloy triangle. BLS in general builds upon the fact that light can be inelastically scattered by magnons [78]. In this scattering process the total energy and the total momentum are conserved. From the energy difference between the incident and scattered light the frequency of the spin wave and from the difference in momentum the wave vector of the magnon can be inferred. One can show that the intensity of the scattered light is proportional to the intensity of the dynamic magnetization [79].

In microBLS a higher spatial resolution compared to standard BLS is achieved by sacrificing the sensitivity for the wave vector. The setup is shown in Figure 3.1 and described in detail in [80]. Laser light with a wave length of 532 nm is first linearly polarized. The beam is then formed using an expander and a diaphragm. Afterwards the light is focused onto the sample which is mounted on a x-y-z-stage. The laser spot has a diameter of 250 nm. Permanent magnets allow for the application of a static external magnetic field.

The backscattered light is directed into an interferometer with a polarizing beam splitter. Here it is exploited that the polarization direction of the light is rotated by 90 degrees when it scatters of a spin wave. Also, this fact makes it possible to distinguish magnetic excitations from other collective excitations such as phonons where no rotation takes place. White light in combination with a CCD camera is used to control the position of the sample and the laser spot.

microBLS can be operated in different measurement modes. BLS spectra can acquired at the position of the laser spot with a frequency resolution of 100 MHz. To investigate the two dimensional spatial structure of spin wave modes, the frequency

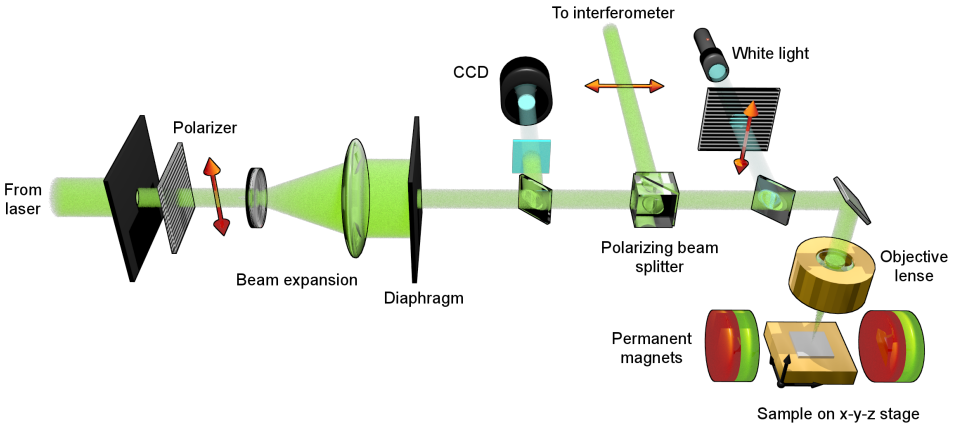

Figure 3.1: microBLS setup. Laser light is focused onto a magnetic sample and inelastically scattered by a magnon. The scattered light is analysed in an interferometer. Figure used by courtesy of Henning Ulrichs [77, p. 33].

can be fixed and the laser spot is then scanned across the sample using the x-y-z-stage. Finally, the excitation pulses can also be synchronized with the interferometer to measure the time development of the spin wave intensity with a time resolution of 1 ns.

3.1.2 Sample

The sample is depicted in Figure 3.2. An equilateral triangle made out of Permalloy (Py), $Ni_{80}Fe_{20}$, with a side length of 2 µm and a thickness of 5 nm was fabricated on top of a 9 nm thick Pt stripline as in detail described in [81]. The test device was produced[1] on sapphire substrates by a combination of room-temperature magnetron sputtering in ultrapure Ar and e-beam lithography. Before deposition, the substrate was annealed in air at 1300 °C, resulting in an atomically smooth surface. In all of the processes involved in the device fabrication, the temperature was kept below 150 °C to minimize interdiffusion at the interfaces.

A magnetic field of $H = 600\,\mathrm{Oe}$ was applied perpendicular to one side of the triangle as shown in the Figure. The field ensures that the ferromagnet is magnetized to saturation. In equilibrium the magnetization then points along the field direction with deviations only at the edges of the sample.

For excitation of the magnetization a dc current I was applied to the Pt layer underneath the Py triangle. The spin Hall effect (SHE) in Pt gives rise to a spin

[1] by S. Urazhdin of Emory University, Atlanta, USA

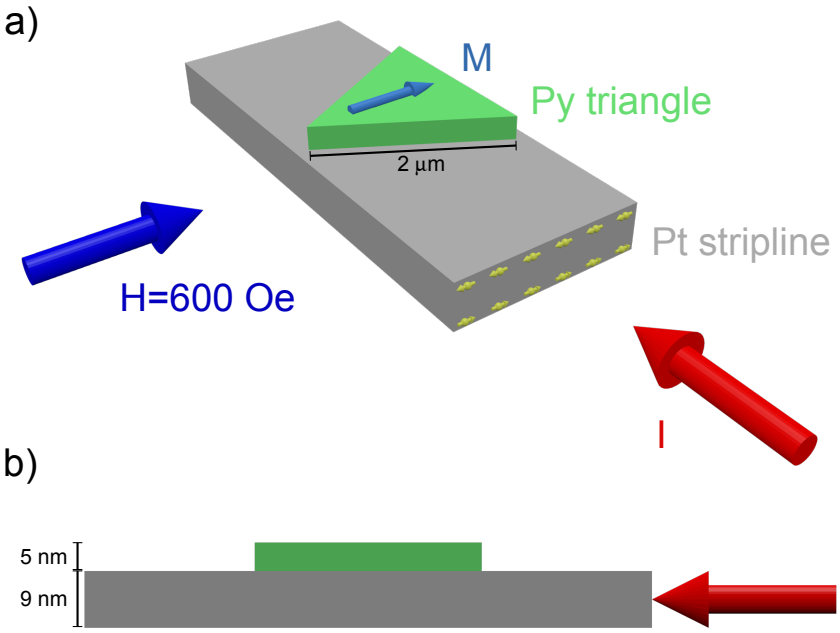

Figure 3.2: Sample. An equilateral triangle with a side length of 2 µm was placed onto a Pt stripline. The width of the stripline is not drawn to scale. The dc current produces a spin imbalance across the Pt layer due to the spin Hall effect.

imbalance perpendicular to the current direction [21, 22, 63]. The current had magnitudes ranging from 0 to 19 mA.

No experimental imaging, e.g. scanning electron microscope images, was available for the sample. Hence, there was no way to verify the sample shape and its dimensions.

3.2 Micromagnetic simulation

3.2.1 Basics

In many cases that are interesting for applications analytical theory of spin waves requires approximations of the nonlinear Landau-Lifshitz-Gilbert-Slonczewski (LLGS) equation [44]. Instead, in micromagnetic simulations the full equation is considered. The basic idea is to map the LLGS onto a discrete mesh and numerically compute the time evolution of the system. Introductions with a focus on nanoscale elements can be found in [82, 83].

In finite-difference simulations the sample is represented by a regular mesh of $N = N_x \cdot N_y \cdot N_z$ prismatic cells $n_1 ... n_N$. This is schematically shown in Figure 3.3. The side length of these cells should be of the order of the exchange length l_{ex}, because in each cell the saturation magnetization M_S as well as the exchange constant A and the Gilbert damping parameter α_G are assumed to be constant [84].

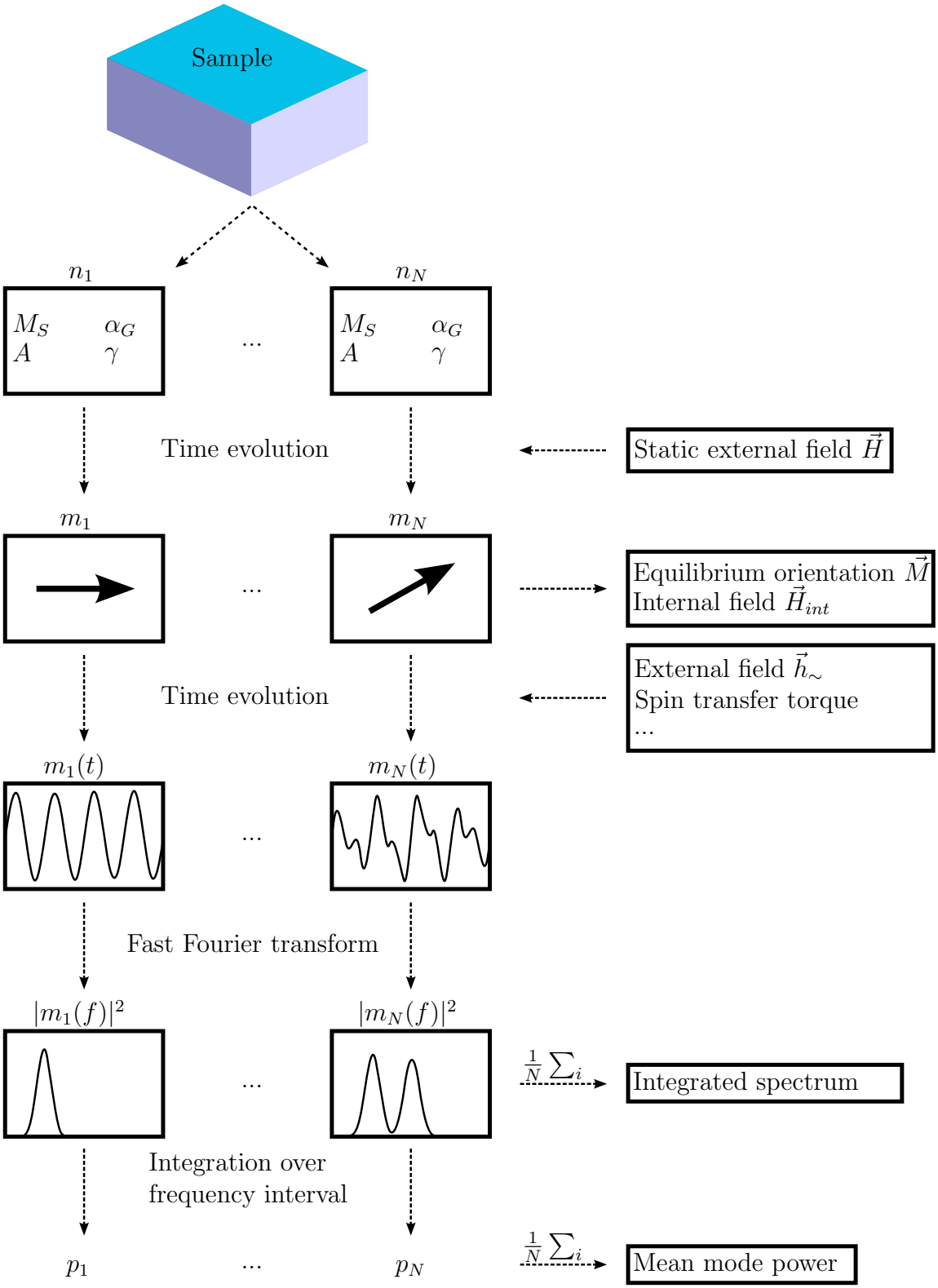

Figure 3.3: Scheme for micromagnetic simulation.

The different energy contributions to the LLGS (see Section 2.1.1) are included in a discrete formalization [84, 85]. In this thesis we use MuMax3, an open source micromagnetic simulation code. Details of the implementation can be found in [86]. We note that the calculation of the dipolar field utilizes spatial Fourier transformation and can therefore be accelerated using graphic cards instead of CPUs [87]. This is the case in Mumax3. Also, the Gilbert damping (2.18) is included up to zeroth order.

We now present the typical steps in micromagnetic simulation and post-processing of the data. Post-processing was done programming the software Wolfram Mathematica [88]. The steps are schematically shown in Figure 3.3. First, the material parameters are set to the typical values for Permalloy: $A = 1.3 \times 10^{-6}\,\mathrm{erg/cm}$, $M_S = 800\,\mathrm{G}$ (equivalent to $4\pi M_S = 10053\,\mathrm{G}$), $\gamma/2\pi = 2.8\,\mathrm{MHz/Oe}$ [58, 89, 90]. The Gilbert damping constant is set to the typical value for Py on Pt of $\alpha_G = 0.02$ [17,19]. This is larger than the standard value of $\alpha_G = 0.008$.

Next, the equilibrium orientation of the magnetization is obtained. For this, a constant external field is applied and an internal relaxation routine of MuMax3 is used before the system is left to relax for 10 ns with an artificially high damping of $\alpha_G = 1$. From this the internal field $\vec{H}_{int}$ can be extracted.

Then, depending on the application, the system is excited by an external magnetic field and/or a spin transfer torque. The system is evolved according to the LLGS for the time t and the time development of each cell is saved at equidistant time steps Δt.

What follows is a generalization of the micromagnetic spectral imaging technique [91]. The time development of each cell $m_1(t)...m_N(t)$ is Fourier transformed to obtain the so called local spectra: $m_i(f) = \mathcal{F}[m_i(t)]$. According to the sampling theorem the maximum frequency is given by $f_{max} = \frac{1}{2\Delta t}$ and the frequency spacing is given $\Delta f = \frac{1}{t}$ [92]. If not stated otherwise, $t = 10\,\mathrm{ns}$ and $f_{max} = 10\,\mathrm{GHz}$.

From the Fourier transformation of each cell two-dimensional maps of the squared absolute value, in short FFT intensity, and the Fourier phase are produced. An integrated spectrum is calculated using

$$|m(f)|^2 = \frac{1}{N}\sum_{i=1}^{N}|m_i(f)|^2, \tag{3.1}$$

which is a measure for the overall strength of a frequency f in the sample.

Spin wave modes appear as peaks in the spectra. The power or energy of a mode can be calculated by numerically integrating over this peak. We then obtain for each cell $p_1...p_N$, which can be again mapped onto a two-dimensional plot. By averaging over the values we get the mean mode power.

In this thesis, two applications are most relevant: eigenmode spectra and the mode power as a function of applied current.

Eigenmode spectra

Here, the system is excited by a field pulse $\vec{h}_{\sim} \perp \vec{M}$ with a length of approximately 15 ps. This excites many modes simultaneously which then exponentially decay due to damping. Each cell is saved every $\Delta t = 50\,\text{ps}$. The integrated spectrum is then analysed and the FFT intensity as well as the phase is mapped out in two dimensions.

Mode power as a function of current

To determine the influence of a current on a mode with frequency f_1 this mode is linearly excited using an rf magnetic field $\vec{h}_{\sim} \perp \vec{M}$ with a time dependence $\sin(2\pi f_1 t)$ and a magnitude of $h_{\sim} = 0.1\,\text{Oe}$. The influence of the current is included using the Slonczewski torque $\vec{\tau}_S$ with a polarization direction $\vec{e_p} = (1, 0, 0)$ and a spin Hall angle $\phi_H = 0.1$ [32, 93, 94]. The system is evolved for 5 ns to reach an equilibrium state and then the magnetization is saved for 10 ns. From this the mode power is obtained as explained above.

3.2.2 Models

In this thesis we have analysed three different micromagnetic model samples that are presented in the following. All models share the typical material parameters of Py. Also, it was verified for each model that a refinement of the mesh did not lead to significant deviations for several test cases. All three models are sketched in Figure 3.4a-c.

Model 1: Square

Model 1 is a square with dimensions of $5 \times 250 \times 250\,\text{nm}^3$, that was descretized into $1 \times 64 \times 64$ cells. Hence, each cell had a size of $5 \times 3.9 \times 3.9\,\text{nm}^3$. A field of $H = 1000\,\text{Oe}$ was applied along the z-direction. Model 1 has the purpose of a reference: The eigenmodes of this geometry are well known and the size is certainly smaller than the decay length as seen in Figure 2.3 [60].

Model 2: Rectangle

Model 2 is a rectangle with dimensions of $10 \times 2000 \times 1730\,\text{nm}^3$, that was descretized into $1 \times 256 \times 256$ cells. Hence, each cell had a size of $10 \times 7.8 \times 6.8\,\text{nm}^3$. A field of $H = 600\,\text{Oe}$ was applied along the z-direction with a slight deviation of 1 degree to avoid degeneracy [93]. Model 2 serves as intermediate between model 1 and model 3. It already has the dimensions of the experimental sample but the geometry is still well known.

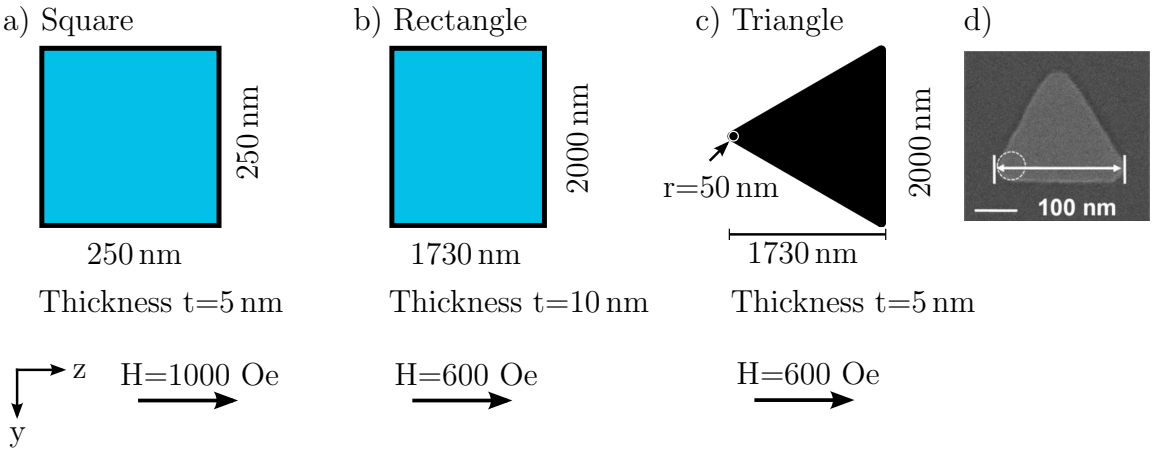

Figure 3.4: Model samples used in this thesis. a) Square **b)** Rechtangle **c)** Triangle **d)** For comparison: Scanning electron micrograph of 300 nm wide, 9 nm thick Py triangle with an average rounding of 70 nm. Figure d) from [95].

Model 3: Triangle

Model 3 comes closest to the experimental sample. It has dimensions of $5 \times 2000 \times 1730\,\mathrm{nm}^3$ and was descretized into $1 \times 256 \times 256$ cells. Hence, each cell had a size of $5 \times 7.8 \times 6.8\,\mathrm{nm}^3$. A field of $H = 600\,\mathrm{Oe}$ was applied along the z-direction with a slight deviation of 1 degree to avoid degeneracy [93].

However, the shape is not a triangle in the mathematical sense as the sharp vertices would not be physical. In the fabrication process vertices with a finite edge radius will be produced as can be seen in Figure 3.4d where an edge radius of 70 nm was found. As no experimental imaging was available we cannot determine the edge radius of our sample and therefore for simplicity assume an edge radius of $r = 50\,\mathrm{nm}$.

4 Results

In the first part of this Chapter we analyse and discuss the experimental data. Then, we develop a micromagnetic model, gradually approaching the experimental situation.

4.1 Experiments

We discuss the spin wave spectrum and investigate how the energy of the spin current flows into different modes.

4.1.1 Spin wave spectrum

The thermal spectrum, meaning the BLS spectrum acquired without any current applied to the sample, is shown in Figure 4.1. We recall that the BLS intensity is proportional to the intensity of the dynamic magnetization. Both spectra are normalised separately. At the center of the triangle (black dots) we see a peak at $f = 7.2\,\mathrm{GHz}$. The peak is not Lorentzian. It is asymmetric with the slope on the left of the maximum being steeper than on the right of the maximum. Also, we see a small shoulder at about 6.0 GHz. This already indicates that this peak originates not from one single spin wave mode but from a superposition of several modes.

At the edge of the sample a new, much larger shoulder appears at frequencies below 6.2 GHz with a maximum at $f = 5.4\,\mathrm{GHz}$. From the dispersion relation (2.12) for a

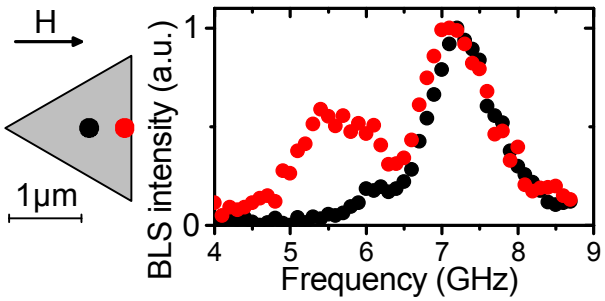

Figure 4.1: Thermal spectrum. Normalised BLS spectra at the edge (red) and in the center (black) of the triangle.

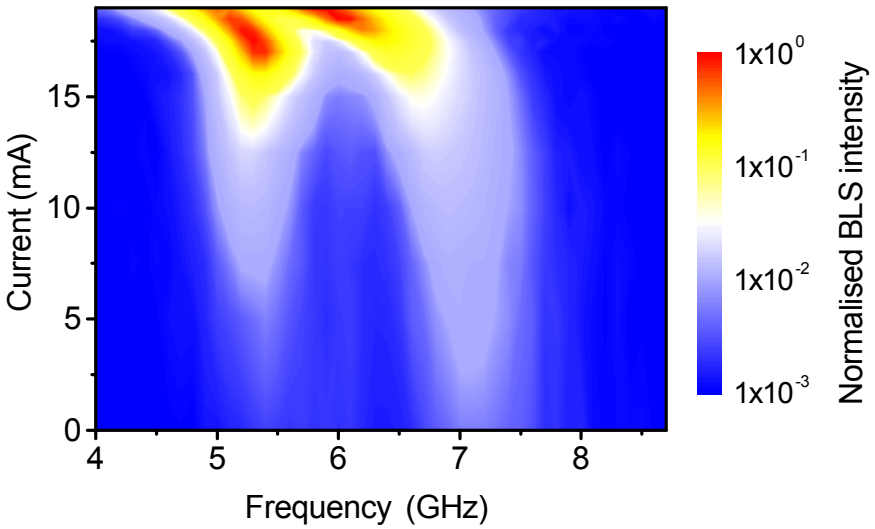

Figure 4.2: BLS spectra as a function of charge current. Pseudocolour logarithmic map of the BLS intensity versus frequency and current. The BLS laser spot was positioned at the edge of the triangle as indicated in the cartoon on the left.

thin film shown in Figure 2.3 we know that the minimum cutoff frequency for this sample should lie at roughly 7.0 GHz. Hence, such low frequencies seen here cannot exist in the center of the triangle. This as well the appearance of the shoulder at the edge gives evidence that the shoulder belongs to the band of edge modes in this sample [57].

Hence, in contrast to most previous studies the triangle is a multi-mode spin wave system which in the following will be subjected to a spin current.

4.1.2 Effect of the spin current

Spectrum

When a charge current with the correct polarity, the one for which the magnetic moments in the spin current are antiparallel to the magnetization, is applied to the sample both edge and center modes can be amplified. This is shown in Figure 4.2. In contrast to theoretical predictions both types of modes are present over the whole current range from 0 to 19 mA. In this range their intensity increases by three orders of magnitude.

However, the behaviour of the intensity as a function of current is quite different for both mode systems. At $I = 0\,\mathrm{mA}$ the center modes are stronger than the edge modes. This difference is compensated at $I = 10\,\mathrm{mA}$. Between 10 mA and 18 mA the edge modes show a stronger intensity - with the maximum difference being about one order of magnitude at $I \approx 17\,\mathrm{mA}$. Above 18 mA the situation is again reversed with the center modes being strongest.

Both edge and center modes exhibit a redshift of the central frequency with the strongest for currents $I > 15\,\mathrm{mA}$. The shift is stronger for center modes.

Spatial behaviour

Two-dimensional mode profiles were recorded by scanning the BLS laser spot over the sample with a step size of $0.1\,\mu\mathrm{m}$ whilst keeping the frequency fixed. Figure 4.3 shows the resulting maps at the edge modes (left) and the center modes (right) peak frequencies for currents of $I = 15\,\mathrm{mA}$, $I = 17\,\mathrm{mA}$ and $I = 19\,\mathrm{mA}$. The mode profiles confirm the assignment of the low frequency peak to edge modes and the high frequency peak to center modes.

The edge modes are situated at the edge that is perpendicular to the magnetic field direction and in the cross section a peak about $0.3\,\mu\mathrm{m}$ away from the edge can be seen. With increasing current the modes profile changes from a triangular shape to a more sinusoidal one. In the direction perpendicular to the magnetic field the modes show two peaks, each being about $0.4\,\mu\mathrm{m}$ away from the closest vertex. In the middle there is a dip that gets less pronounced with increasing current.

The center modes are extended across the whole of the triangle. Along the direction of the field the intensity increases from the apex to the edge and has a maximum $0.6\,\mu\mathrm{m}$ away from the edge. For increasing current this peak gets more pronounced. In the direction perpendicular to the field a dip is seen in the middle that vanishes for $I = 19\,\mu\mathrm{m}$. We stress that the center modes do not show three-fold symmetry and therefore cannot be described by the eigenfunctions of the triangular geometry in contrast to the center modes in rectangular elements [60, 96, 97]. A more detailed discussion will be presented lateron.

From these spatial BLS measurements we can conclude that the spatially uniform spin current influences the modes in a spatially non-uniform way - at least in the current range from 15 to 19 mA. There are two explanations at hand. We recall that we are most likely imaging a superposition of several spin wave modes. The changes in the profile might originate from a different amplification of different modes, thus altering the superposition, or from a true change in the spatial mode structure. This point is discussed further lateron.

Quantitative analysis

To quantify the behaviour of the current excited modes we fitted the BLS spectra. From the fits we extracted the area under each peak, which is proportional to the power of the modes, and the central frequency. All fits were performed using the software Fityk employing a least-square method [98]. Fits with simple Lorentzian curves did not produce satisfying results as they were not able to incorporate the asymmetry seen in the peaks [99]. Instead we used a split pseudo-Voigt function that is often utilized for spectroscopic analysis [100]. The pseudo-Voigt function is

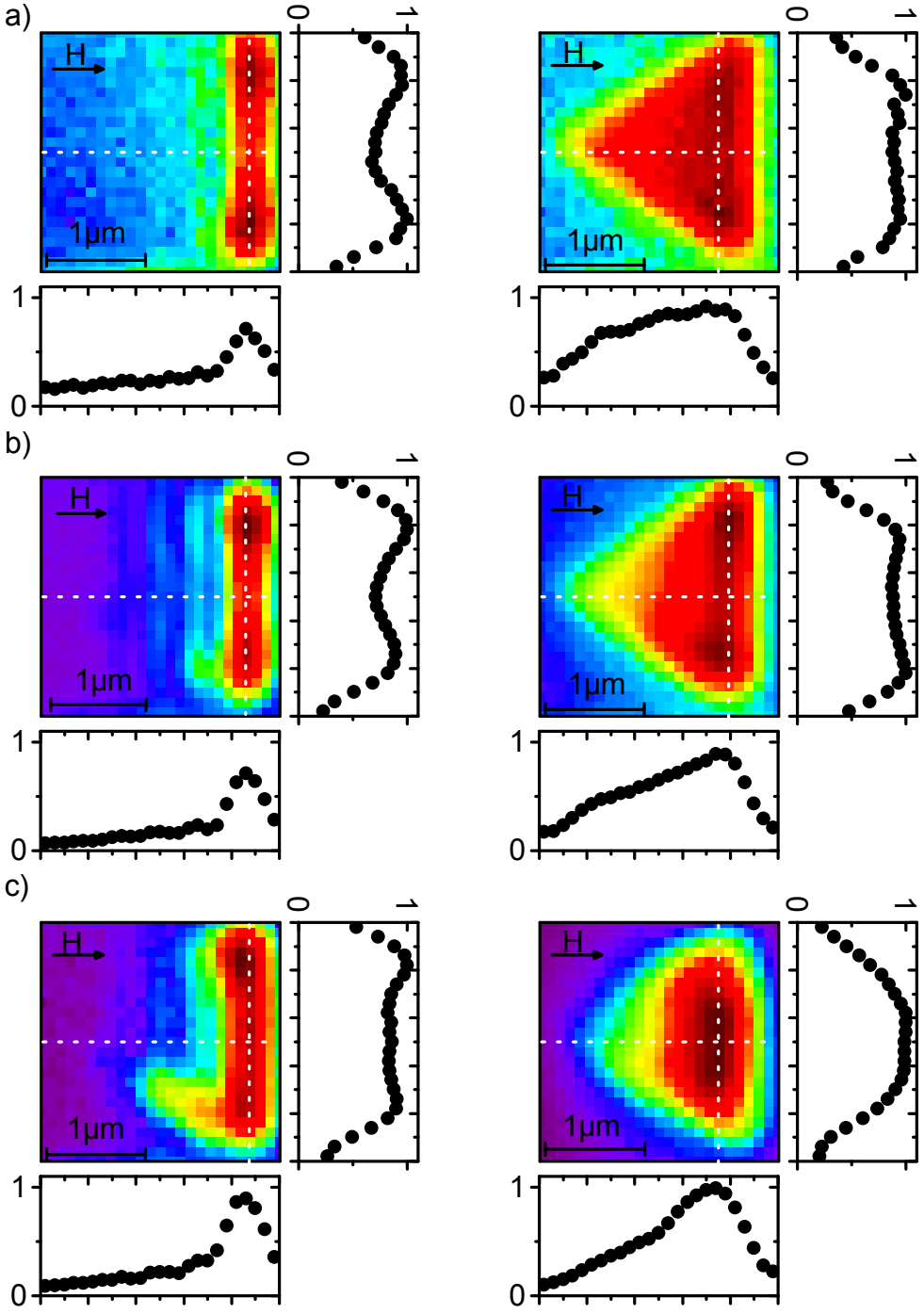

Figure 4.3: Spatial BLS maps. BLS intensity across the triangle at the edge modes peak frequency (left) and the center modes peak frequency (right) at currents of **a)** $I = 15\,\mathrm{mA}$, **b)** $I = 17\,\mathrm{mA}$ and **c)** $I = 19\,\mathrm{mA}$.

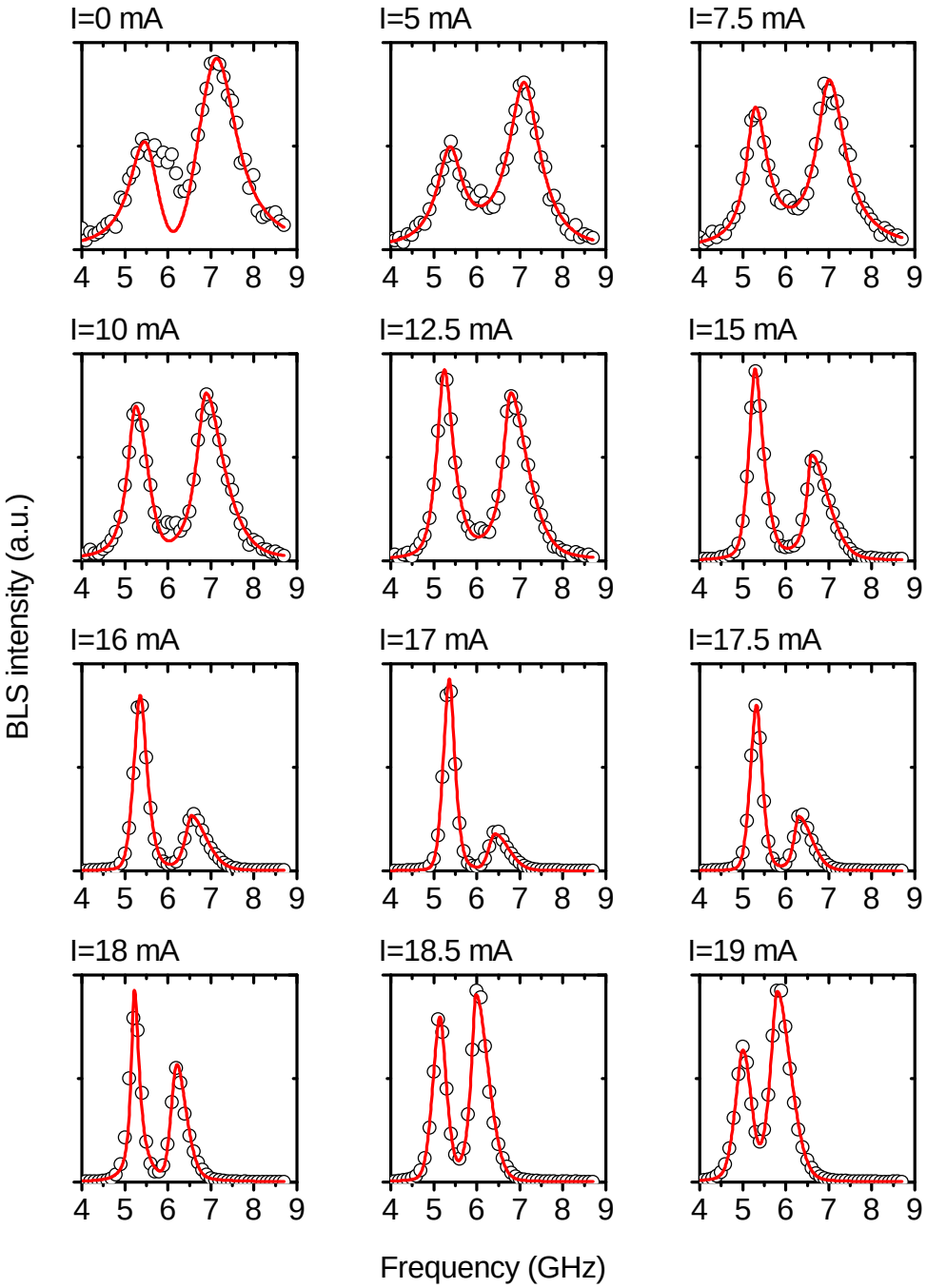

Figure 4.4: Fitting of the whole spectrum. Normalised BLS spectra at the edge of the triangle for different currents. Solid lines show fits with a superposition of two split Pseudo-Voigt functions.

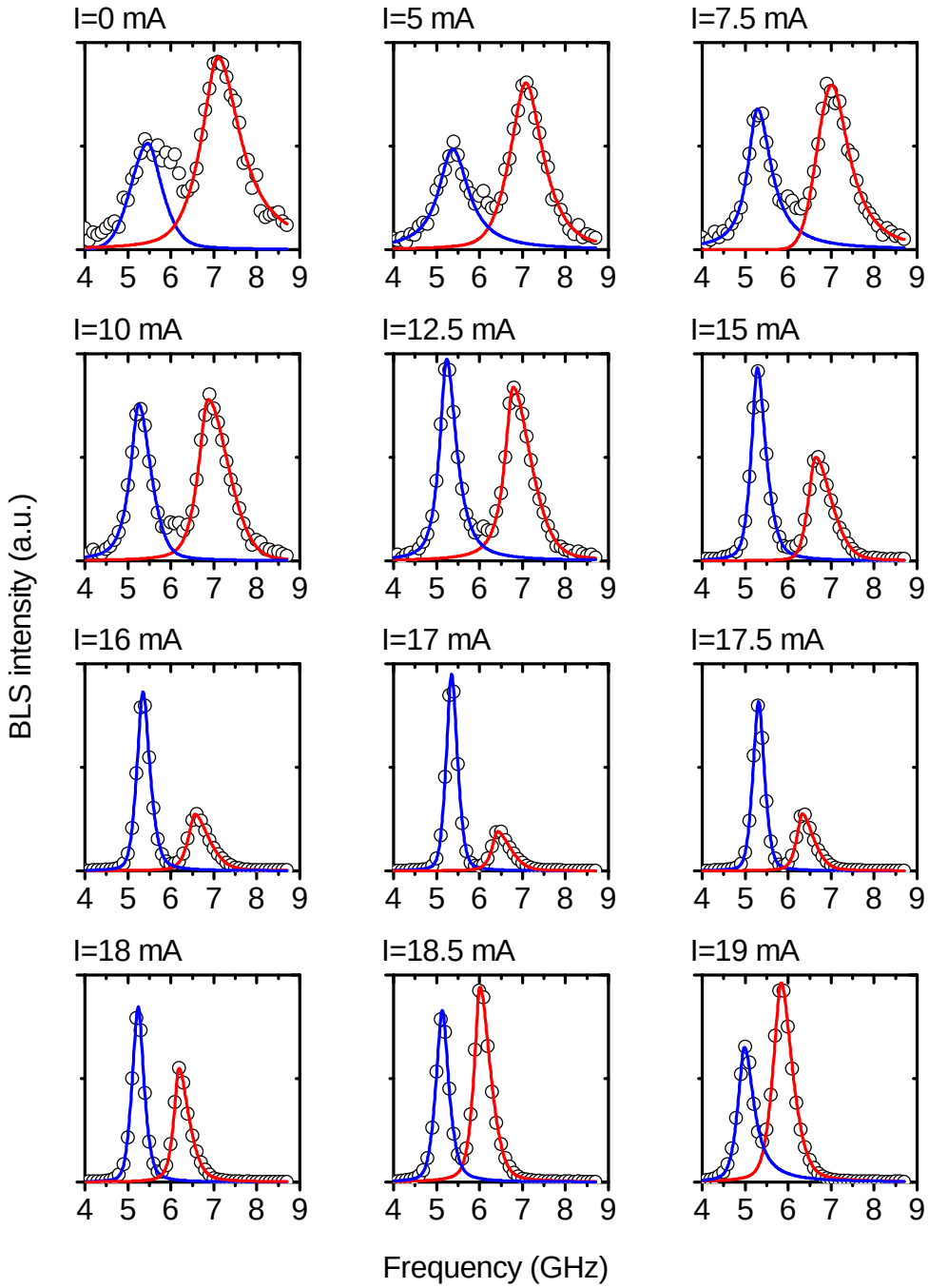

Figure 4.5: Separate fitting of center and edge modes. Normalised BLS spectra at the edge of the triangle for different currents. Solid lines show fits where each peak is separately fitted with a split Pseudo-Voigt function.

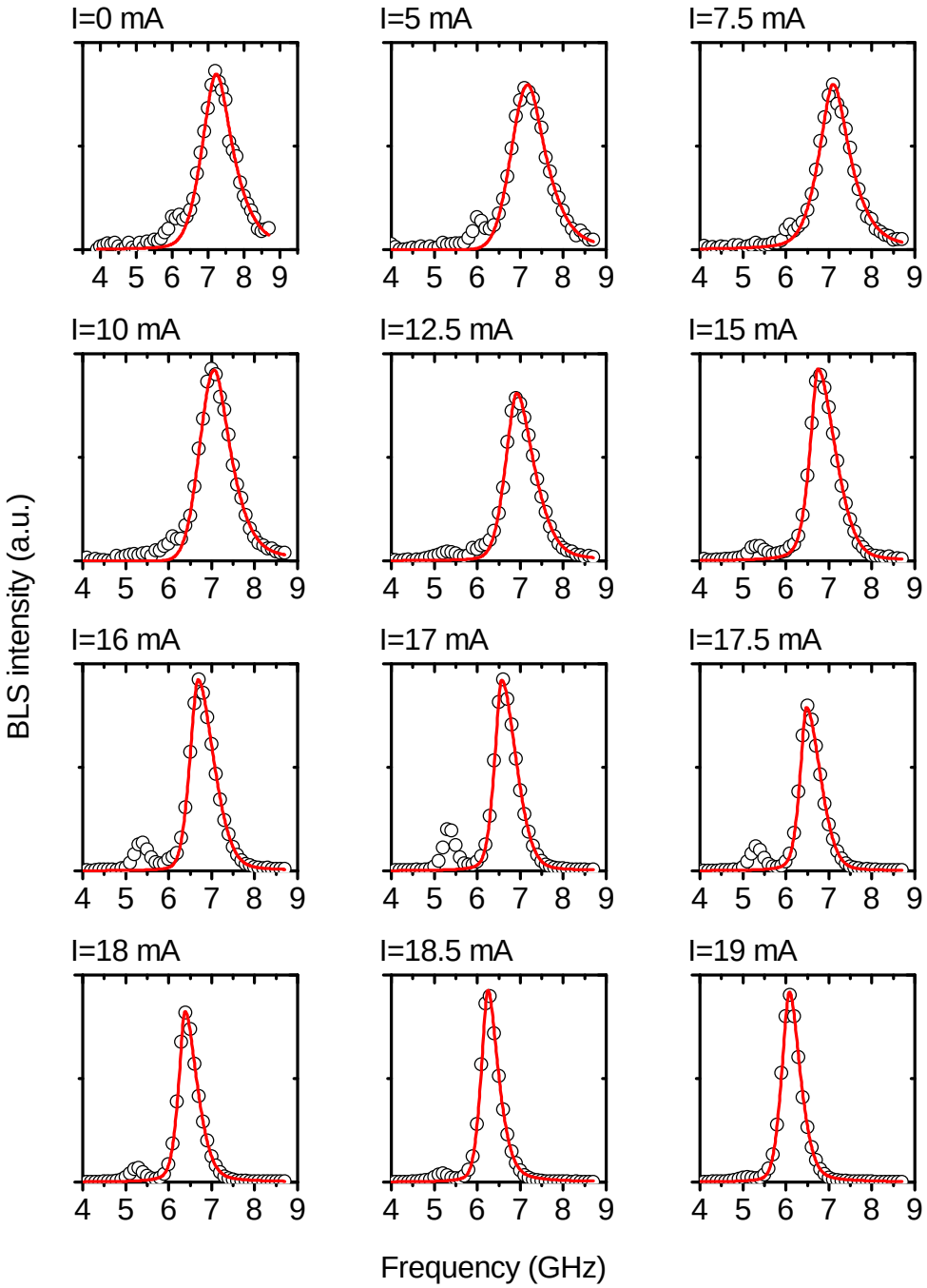

Figure 4.6: Fitting of center modes at the center. Normalised BLS spectra at the center of the triangle for different currents. Solid lines show fit to the center mode peak with a split Pseudo-Voigt function.

given by the superposition of a Gaussian and and a Lorentzian function:

$$PV(f_c, I_0, A, \eta) = I_0 \left[(1-\eta) \exp\left(-\left(\frac{\ln(2)(f-f_c)}{\sigma\sqrt{\pi}} \right)^2 \right) + \eta \frac{1}{1+\left(\frac{f-f_c}{\sigma}\right)^2} \right] \quad (4.1)$$
$$\text{with } \sigma = \frac{2A}{I_0 \pi}.$$

Here, I_0 is the intensity at the central frequency f_c and A is the area. η determines the shape with $\eta = 1$ meaning completely Lorentzian and $\eta = 0$ meaning completely Gaussian. A split Pseudo-Voigt function is then used to describe the BLS intensity:

$$I_{BLS}(f) = \begin{cases} PV(f_c, I_0, A_1, \eta_1) & \text{for } f < f_c \\ PV(f_c, I_0, A_2, \eta_2) & \text{for } f \geq f_c. \end{cases} \quad (4.2)$$

We have used three different fitting procedures:

1. We have fitted the spectra obtained at the edge of the triangle (red dot in Figure 4.1). Each spectrum was fitted as a whole. Hence, a superposition of two split pseudo-Voigt functions was assumed, $I_{BLS} = I_{BLS}^{Edge} + I_{BLS}^{Center}$. In Figure 4.4 the spectra and corresponding fit functions are shown. The data can be described well by the assumed model. The largest discrepancies are seen for small currents $I < 10\,\text{mA}$, because thermal noise is still visible. Also, we see that the edge mode shoulder evolves into a single peak and not all edge frequencies are amplified, which makes the fitting at small currents difficult.

2. As an alternative approach we have fitted the spectra obtained at the edge (red dot in Figure 4.1) with two separate functions, one for the edge and one for the center modes. The results are shown in Figure 4.5. Again we find good agreement between model and data. However, this approach is likely to overestimate the area under the edge peak, because the tail of the center peak is incorporated in there.

3. We have fitted the center peak in the BLS spectra obtained at the center of the triangle (black dot in Figure 4.1). A fitting of the edge peak was not possible, because the edge modes were only present in a limited current range. Figure 4.6 presents the data and the fits, again showing good agreement.

Figure 4.7 compares the fitting procedures 1 and 2 for the spectra obtained at the edge. On the left the inverse power is shown given by the inverse area normalised at zero current. For all modes and in both fitting procedures we see a similar trend. From 0 to 5 mA the inverse power sharply decreases. Between 5 mA and 16 mA the decrease is roughly linear, sometimes slightly concave. Also, the central frequency decreases with increasing current. The non-linear decrease originates from the reduction of the effective magnetization due to the excitation [28].

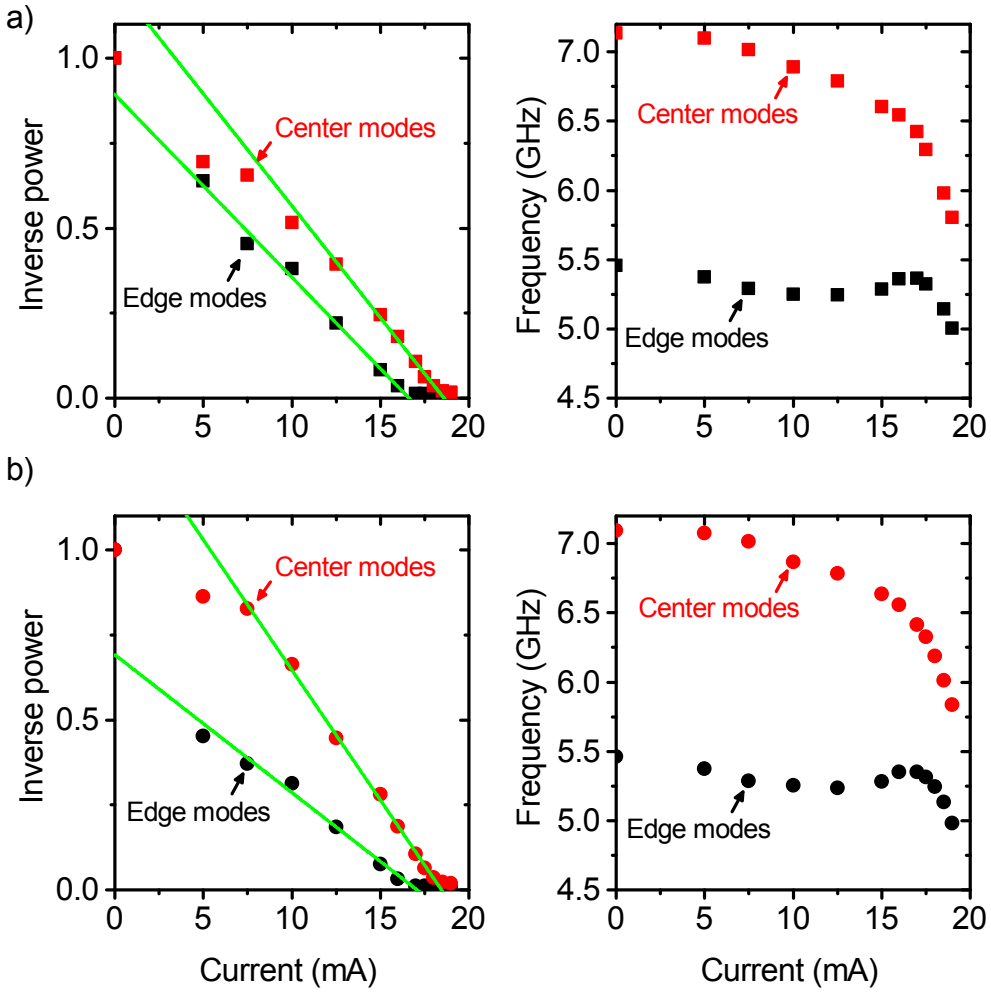

Figure 4.7: Fitting results of spectra at the edge. Normalised inverse power and central frequency f_c as a function of current as determined from the fitting of the BLS spectra acquired at the edge of the triangle: **a)** edge and center modes fitted together and **b)** edge and center modes fitted separately. Solid green lines are linear fits.

Strictly speaking, the non-linear auto-oscillator theory presented earlier (Equation (2.32)) is no longer valid, because the assumption that only one spin wave mode is excited no longer holds. Still we observe the linear decrease predicted by Equation (2.32) in a limited current range. We can extrapolate these linear regions to 0 using linear fits and extract I_{th}. However, we stress that these are collective thresholds for *all* center modes and for *all* edge modes, which are probed by the microBLS setup. No conclusion can be made for the threshold of a *single* mode.

For the edge modes we find $I_{\mathrm{th}} = 16.5\,\mathrm{mA}$ for fitting procedure 1 and $I_{\mathrm{th}} = 17.0\,\mathrm{mA}$ for fitting procedure 2. For the center modes we find $I_{\mathrm{th}} = 18.6\,\mathrm{mA}$ and $I_{\mathrm{th}} = 18.5\,\mathrm{mA}$. The ratio of these values is given by

$$\rho_{exp} = \frac{I_{\mathrm{th}}^{center}}{I_{\mathrm{th}}^{edge}} \frac{18.55\,\mathrm{mA}}{16.75\,\mathrm{mA}} \approx 1.11, \tag{4.3}$$

where we have used the average value for both mode systems. On the other hand, from the theoretical Equation (2.31), assuming that σ_0 is equal for all modes, we see that the ratio of threshold currents solely depends on the relaxation frequencies:

$$\rho_{the} = \frac{\omega_r^{center}}{\omega_r^{edge}} = \frac{\alpha_G \omega^{center} \frac{\partial \omega^{center}}{\partial \omega_H}}{\alpha_G \omega^{edge} \frac{\partial \omega^{edge}}{\partial \omega_H}} \approx \frac{f^{center} \frac{\Delta f^{center}}{\Delta H}}{f^{edge} \frac{\Delta f^{edge}}{\Delta H}} \approx 1.25. \tag{4.4}$$

Here, the field dependence of the mode frequencies was extracted from a BLS measurement at $H = 1000\,\mathrm{Oe}$ yielding $\Delta H = 1000\,\mathrm{Oe} - 600\,\mathrm{Oe} = 400\,\mathrm{Oe}$ and

$$\Delta f^{center} = f^{center}(H = 1000\,\mathrm{Oe}) - f^{center}(H = 600\,\mathrm{Oe}) = 9.2\,\mathrm{GHz} - 7.1\,\mathrm{GHz} = 2.1\,\mathrm{GHz} \tag{4.5}$$

$$\text{and } \Delta f^{edge} = f^{edge}(H = 1000\,\mathrm{Oe}) - f^{edge}(H = 600\,\mathrm{Oe}) = 7.6\,\mathrm{GHz} - 5.4\,\mathrm{GHz} = 2.2\,\mathrm{GHz}. \tag{4.6}$$

Qualitatively, the idea that modes with a higher frequency have a higher threshold current (due to $\omega_{\mathrm{r}} \propto \omega$) is confirmed by the data. Quantitatively, the values differ by about 13 % and the different thresholds cannot be explained by different frequencies alone.

In Figure 4.8a the inverse power and central frequency for fitting procedure 3 for the center modes measured at the center of the triangle are shown. We find a linear dependence for $I \geq 5\,\mathrm{mA}$ yielding a threshold current $I_{\mathrm{th}} = 19.5\,\mathrm{mA}$. Hence, the threshold current of the center modes depends on the position. However, the different central frequencies, $f = 7.1\,\mathrm{GHz}$ at the edge and $f = 7.2\,\mathrm{GHz}$ at the center, already indicates that different modes are probed, so a comparison is difficult. The central frequency also shows a strongly non-linear decrease.

All fitting results are compared in Figure 4.8b. We point out that the central frequencies obtained from the spectra at the edge of the triangle (procedure 1 and 2) are independent of the fitting procedure indicating that the fits converge in a robust

manner. The result that the edge modes are affected differently compared to the center modes holds regardless of the fitting procedure. Over a wide current range up to $I = 18\,\mathrm{mA}$ the inverse power of the edge modes lies below the center modes showing that the relative growth of the power of these modes has been stronger. The difference is larger for fitting procedure 2, because as mentioned it overestimates the area under the edge mode peak and therefore enhances the effect. The effect cannot be explained by different relaxation frequencies alone.

When the current approaches I_{th} for both mode systems auto-oscillations should be excited [38]. Instead the power of the modes saturates as previously observed in other non-local spin injection geometries [23, 27, 28]. The reason for this is that close to I_{th} additional relaxation channels are created through which the energy decays, mainly scattering with large wave vector, exchange dominated spin waves, which occupy a rather large phase volume.

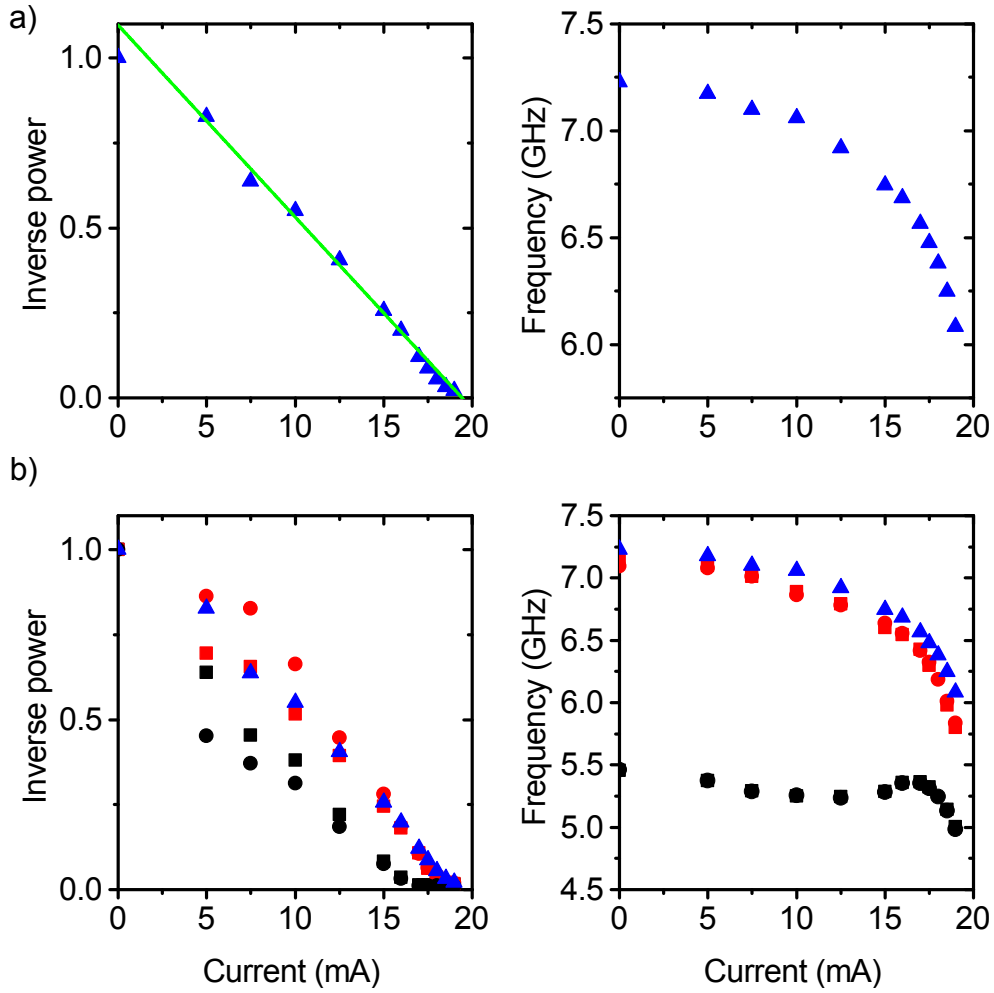

Figure 4.8: Fitting results of spectra at the center and comparison of all results. a) Normalised inverse power and central frequency f_c as a function of current as determined from the fitting of the BLS spectra acquired at the center of the triangle. Solid green line is a linear fit. **b)** Comparison of fitting results for all three fitting procedures. Symbols and colours are the same as used in Figure 4.7 and 4.8a.

4.2 Micromagnetic simulation

We describe the results of the micromagnetic simulations of spin wave spectra and current excited dynamics for the models discussed in the Chapter 3.

4.2.1 Spin wave spectrum

Spin wave spectra are obtained using the method described in Section 3.2.1.

Square

We use model 1 to show the capabilities of the micromagnetic spectral imaging technique [91]. In Figure 4.9 all dynamics were excited with a field pulse $\vec{h_\sim} \perp \vec{H}$ with an amplitude of $h_\sim = 40\,\mathrm{Oe}$. The spatial profile of the exciting field was varied to be able to excite higher order modes, which otherwise cannot (or only with low efficiency) be excited with a uniform field [91]. The spatial profiles, assuming that the origin of the coordinate system lies at the center of the square, are given by:

$$
\begin{aligned}
a)\ \vec{h}_\sim &= h_\sim \cos\left(\frac{\pi}{l_z} z\right) \cos\left(\frac{\pi}{l_y} y\right) \vec{e_y}, \\
b)\ \vec{h}_\sim &= h_\sim \sin\left(\frac{\pi}{l_z} z\right) \sin\left(\frac{\pi}{l_y} y\right) \vec{e_y}, \\
c)\ \vec{h}_\sim &= h_\sim \cos\left(\frac{\pi}{l_z} z\right) \cos\left(\frac{3\pi}{l_y} y\right) \vec{e_y}.
\end{aligned}
$$

In a) we get the typical result for the fundamental mode which has no nodal lines. The frequency is given by $f_1 = 9.8\,\mathrm{GHz}$. The intensity has a single peak at the center and the phase is constant throughout the sample meaning that all magnetic moments precess in phase.

For b) we find a frequency of $f_2 = 11.4\,\mathrm{GHz}$. The mode has one nodal line in each direction. We see that the lobes oscillate in phase in groups of two with a phase difference of π between the two groups.

The third mode c) has a frequency of $f_3 = 12.8\,\mathrm{GHz}$ with two nodal lines in y-direction and no lobes along the field direction. Top and bottom lobe oscillate in-phase, the middle lobe is out of phase by π.

We can rationalize the order of the modes in frequency space by looking at the dispersion in Figure 2.3. Due to the small thickness ($L = 5\,\mathrm{nm}$) an increase of nodal lines, meaning higher k, in the relevant range always leads to an increase of the mode frequency. However, for nodal lines in the direction of the field $\vec{k} || \vec{H}$ this increase is smaller than perpendicular to it, $\vec{k} \perp \vec{H}$. This explains why $f_3 > f_2$ although both modes have two nodal lines.

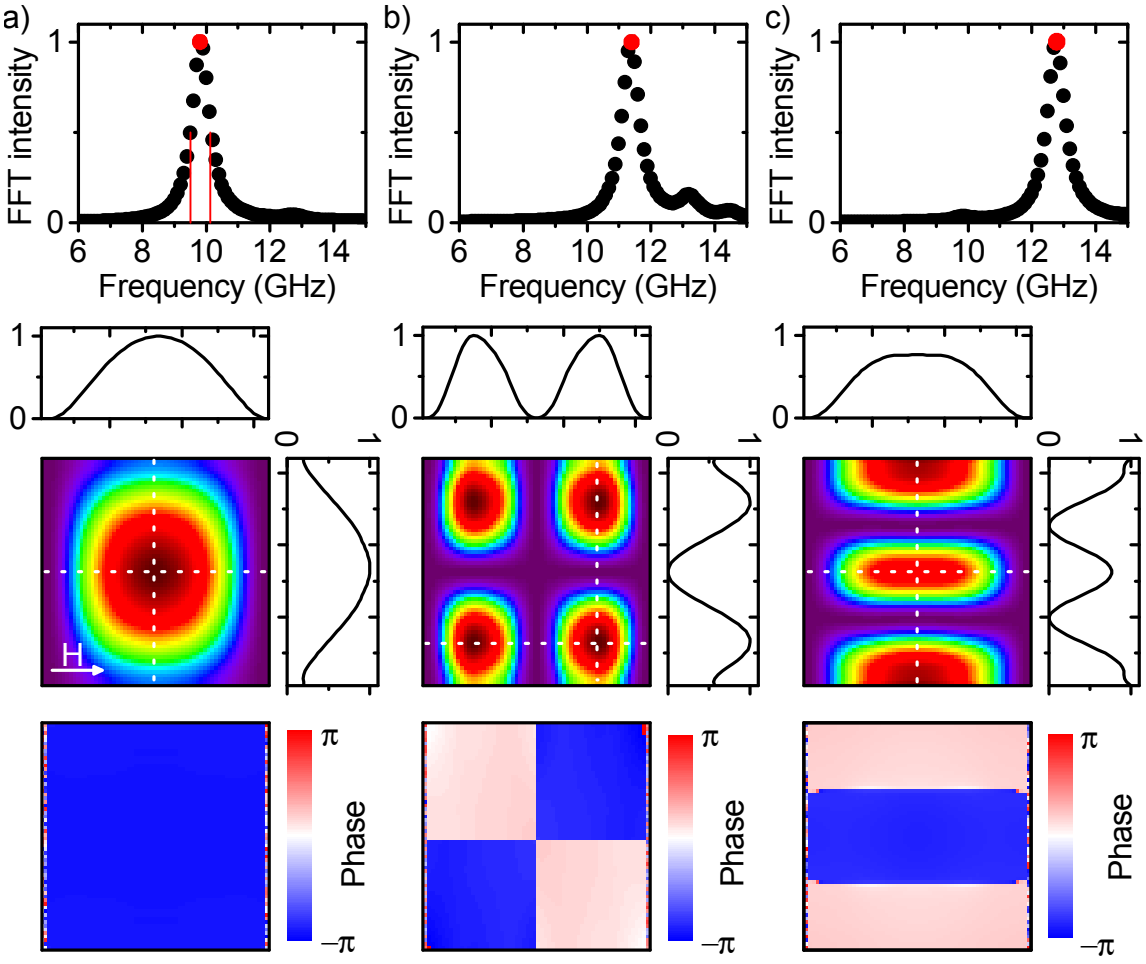

Figure 4.9: Three different modes in the Py square. Averaged spectrum, intensity and phase maps for **a)** the fundamental mode without nodal lines and **b) and c)** higher order modes with two nodal lines. Dotted lines correspond to the cross sections shown in the line plots.

Rectangle

With model 2 we keep the mirror symmetry of model 1 along the y and z axis, but already adapt the lateral dimensions of the triangle used in the experiments. For the equilibrium magnetization of this structure in a field of 600 Oe we found a flower state [101] regardless of the initial magnetization before relaxation. However, in experiments this state is usually not observed and rather c-states are found [102–104]. The energy difference between the two states is small [59, 101]. Also, the flower state was unstable with respect to domain wall motion when a thermal fluctuation field corresponding to a temperature $T = 300\,\mathrm{K}$ was included. This domain wall motion also showed up in $T = 0\,\mathrm{K}$ simulations including a spin-transfer torque and absorbed large amounts of energy as well as interfering with the edge modes. We therefore artificially created a c-state by fixing the magnetic moments of the first and the last column of simulation cells to be directed in the $\pm y$-direction as shown in Figure 4.10a. This effectively leads to a pinning of the magnetization, which for a large width-to-thickness ratio is the correct boundary condition [105]. The c-state was stable with respect to room temperature conditions. The same behaviour was observed for the model of the triangle and therefore the simulation cells were also fixed in that model.

The internal field in the c-state configuration is shown in Figure 4.10a. The field is nearly homogeneous along the y-direction and in the central region along the z-direction. About 0.4 µm away from the edge the internal field starts to decrease and reaches zero at the edges as described in Section 2.1.3.

The dynamics were excited with a uniform field pulse $\vec{h}_{\sim} \perp \vec{H}$. The corresponding averaged spectrum is shown in Figure 4.10b. We see a peak at $f = 7.1\,\mathrm{GHz}$ and and shoulder reaching down to $f \approx 6.0\,\mathrm{GHz}$. Compared to the square (model 1) these frequencies are lower, which can be explained by the larger lateral size of model 2 as well as a lower static external field. The FFT intensity maps at $f = 7.2\,\mathrm{GHz}$ and $f = 6.2\,\mathrm{GHz}$ are shown in Figures 4.10c and d, respectively. These correspond to the strongest peaks in the local spectra at the center and at the right edge of the rectangle.

The intensity at $f = 7.2\,\mathrm{GHz}$ resembles the fundamental mode of model 1. The phase map shows a constant phase across the region of homogeneous internal field supporting this assignment. The intensity shows an approximately sinusoidal dependence in both y- and z-direction. In z-direction several deviations from a cos^2-profile corresponding to the decrease of the internal field are seen. Also, the profile is asymmetric, which is caused by the slight asymmetry of the external field. In general, we find that model 2 and 3 are sensitive to even small misalignments of the external field, probably due to the small thickness. We have kept the misalignment, because the experimental data is also slightly asymmetric (Figure 4.3) and exact symmetry is not to be expected from experiment.

At $f = 6.2\,\mathrm{GHz}$ the intensity is located in the region of reduced internal field. Hence, these are the lowest order edge modes [59]. Note that the strongest peak in the local spectrum at the left edge of the sample lies at $f = 6.1\,\mathrm{GHz}$. This indicates

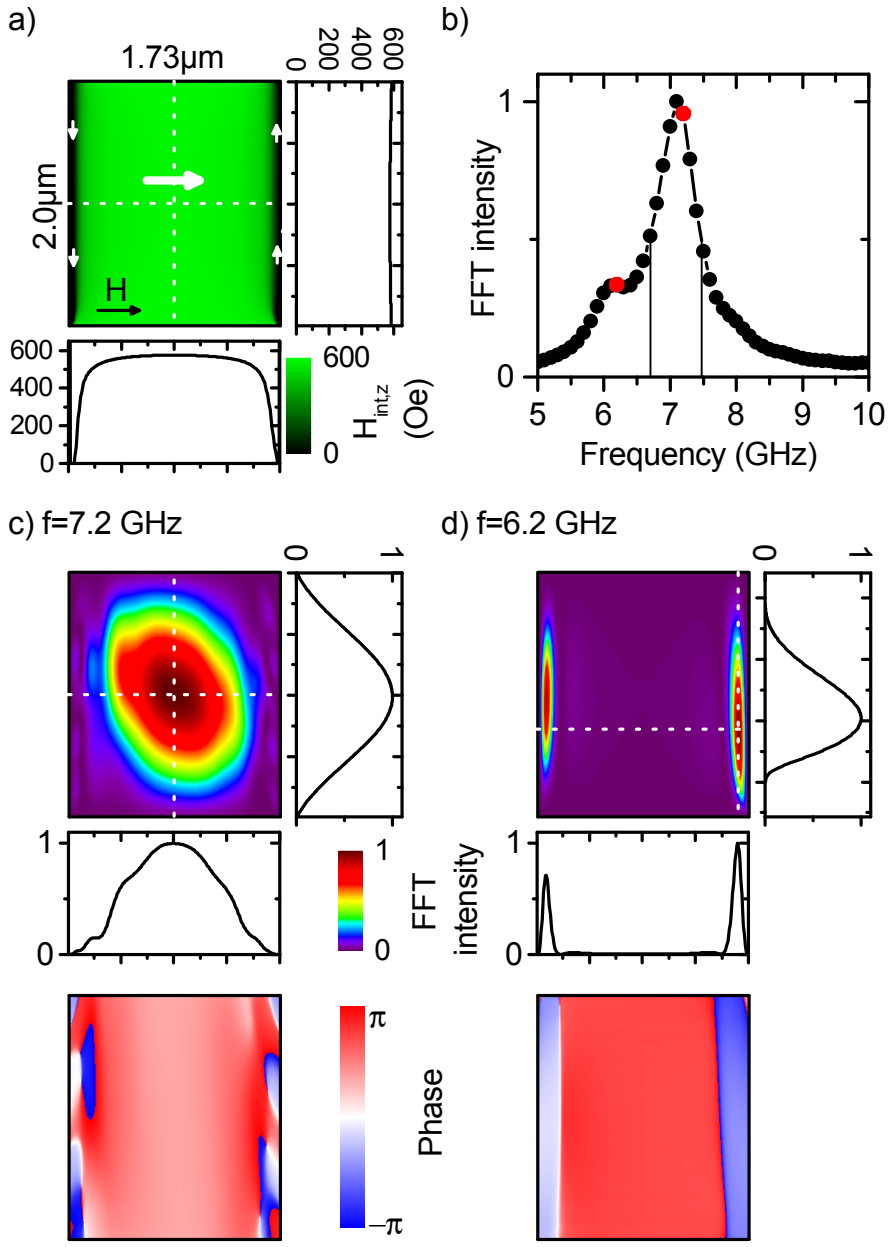

Figure 4.10: Spectrum of the Py rectangle. a) Pseudocolour map of the z-component of the internal field H_{int}. White arrows indicate the equilibrium orientation of magnetization in the s-state. **b)** Normalised averaged spectrum. Red dots correspond to intensity and phase maps at **c)** $f = 7.2\,\mathrm{GHz}$ and **d)** $f = 6.2\,\mathrm{GHz}$. Dotted lines correspond to the cross sections shown in the line plots.

that the two modes are independent, which is further corroborated by the different phase.

We now investigate the transition from a rectangular to a triangular sample by decreasing the length of the left side of the rectangle (Figure 4.11). We lower the damping to $\alpha_G = 10^{-5}$ to be able to distinguish between different modes due to a smaller linewidth. Dynamics were again excited using a uniform field pulse $\vec{h_\sim} \perp \vec{H}$. In Figure 4.11 we show, from left to right, the micromagnetic model and the FFT intensity maps at the peak frequency in the local spectra at the left edge, the right edge and in the center.

For the rectangle we reproduce Figure 4.10 with slight downwards shift of the edge mode frequencies due to the smaller damping. The center mode now occupies less area indicating that with $\alpha_G = 0.02$ we have actually been imaging a superposition of modes rather than one single mode. By decreasing the length of the left side l the intensity profiles and frequencies change:

- **The left edge mode** sees an increase in frequency from 6.0 GHz to 8.2 GHz. This can be explained by the decreasing localization length of the mode in the y-direction which leads to a larger characteristic wave vector. We see that for $l \leq 0.25$ µm the mode lies in the frequency range of center modes (meaning above the FMR frequency $f_0 = \omega_0/2\pi \approx 7.1$ GHz). The mode continuously evolves from an edge mode to a so called apex mode or corner mode [106].

- **The right edge mode** has a constant frequency. Its localization length also decreases slightly, because with decreasing l the boundaries in y direction come closer.

- **The strongest center mode** keeps its fundamental mode shape until $l = 0.5$ µm. However, the peak intensity moves towards the apex of the triangle and consequently the frequency increases from 7.2 GHz to 7.8 GHz due to a smaller localization length and thus larger characteristic wave vector in the y-direction. For $l = 0.125$ µm the former center mode merges with the apex mode. The strongest center mode peak is then found at $f = 7.3$ GHz. Whereas before the development could be understood as a continuous evolution, we see a distinct change in the mode profile. The mode has its peak at the same position as the mode for $l = 1.0$ µm, but now its intensity decays towards the base of the triangle indicating that the spectrum has become quasi-continuous [106, 107].

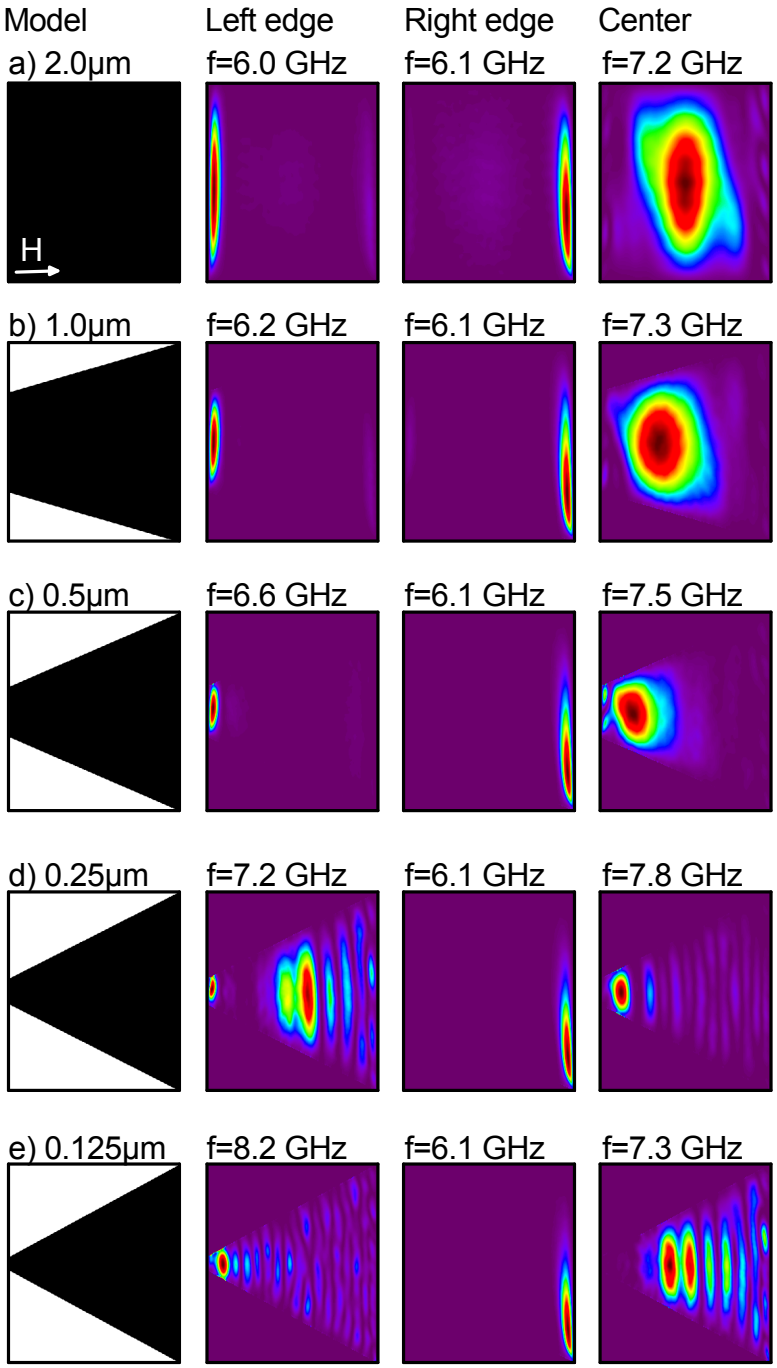

Figure 4.11: Evolution of the spin wave spectrum from a rectangle to a triangle. Model with length of left side indicated and FFT intensity maps. Intensity maps show the mode structures corresponding to the strongest frequencies at the left edge, at the right edge and in the center. Frequencies are indicated above the maps.

Triangle

A quasi-continuous spectrum is found in the triangle (model 3). The internal field is shown in Figure 4.12b. As before the internal field is maximal at the the center with $H_{\mathrm{int,z}} = 585\,\mathrm{Oe}$ and decreases to zero at the apex and the base. We see that the two other sides of the triangle suffer from a staircase artefact due to the prismatic discretization of the shape. There the internal field shows unphysical jumps. As we are not interested in the dynamics there we can neglect this. Compared to the rectangle we see that the decrease of the internal field in z-direction is not symmetric around $z = 0$ at the center. Towards the base the decrease of the field takes place over a range of 0.4 µm, towards the apex over only about 0.2 µm. This is the manifestation in the internal field of a fundamental symmetry breaking: Other than a rectangle a triangle does not show mirror symmetry about the y-axis.

Due to the loss of symmetry it is already clear that the spin wave mode profiles cannot be approximated by the sinusoidal profiles which are the eigenfunctions of a rectangular geometry. One might try to approximate the profiles by the eigenfunctions of a triangle with Dirichlet boundary conditions, which show threefold symmetry [96, 97]. However, this threefold symmetry is broken by the magnetic field and the approach fails as well. Only for an external field $\vec{H} = 0$ the C_3-symmetry is seen in the normal mode profiles [106].

In our simulations the integrated spectrum of the triangle shows a single peak at $f = 7.2\,\mathrm{GHz}$ (Figure 4.12c). The peak has a full width at half-maximum of 1.1 GHz which is nearly double the width of the fundamental mode peak of the square (Figure 4.9a). As the Gilbert damping in both models is the same ($\alpha_G = 0.02$), this increased width has to be caused by a superposition of many modes. A linewidth of 1.1 GHz is in good agreement with the experimental data at $I = 0\,\mathrm{mA}$.

This is confirmed by the intensity and phase maps in Figure 4.12d. We clearly see a continuous spectrum from 6.7 GHz to 7.6 GHz. The peak intensity shifts in position from the base at 6.7 GHz to the apex at 7.6 GHz. Away from the peak position the intensity decays. The increase in frequency can hardly be explained by the internal field profile but rather by the shrinking mode localization length in y-direction. A clear phase relation can only be found for edge modes up to 6.8 GHz. For higher frequencies distinct jumps can be seen even in areas with high intensity, which provides evidence that this is not a standing wave spectrum.

The intensity profiles fit quite well to the experimental results. There we found center modes to be present in the whole of the triangle with a peak towards the base. In the simulation this is seen in a similar way for $7.0\,\mathrm{GHz} \leq f \leq 7.2\,\mathrm{GHz}$.

The spectra depend on the position of extraction: At the center (blue) the peak lies at 7.1 GHz, which is in good agreement with the experimental data (Figure 4.1). At the edge (red) the peak lies at 6.7 GHz, which is considerably higher than edge mode frequency in the experiment of $f \approx 5.4\,\mathrm{GHz}$.

A mismatch between edge mode frequencies in experiment and simulation is quite common [59, 108–111]. There can be several reasons for this, all of which originate

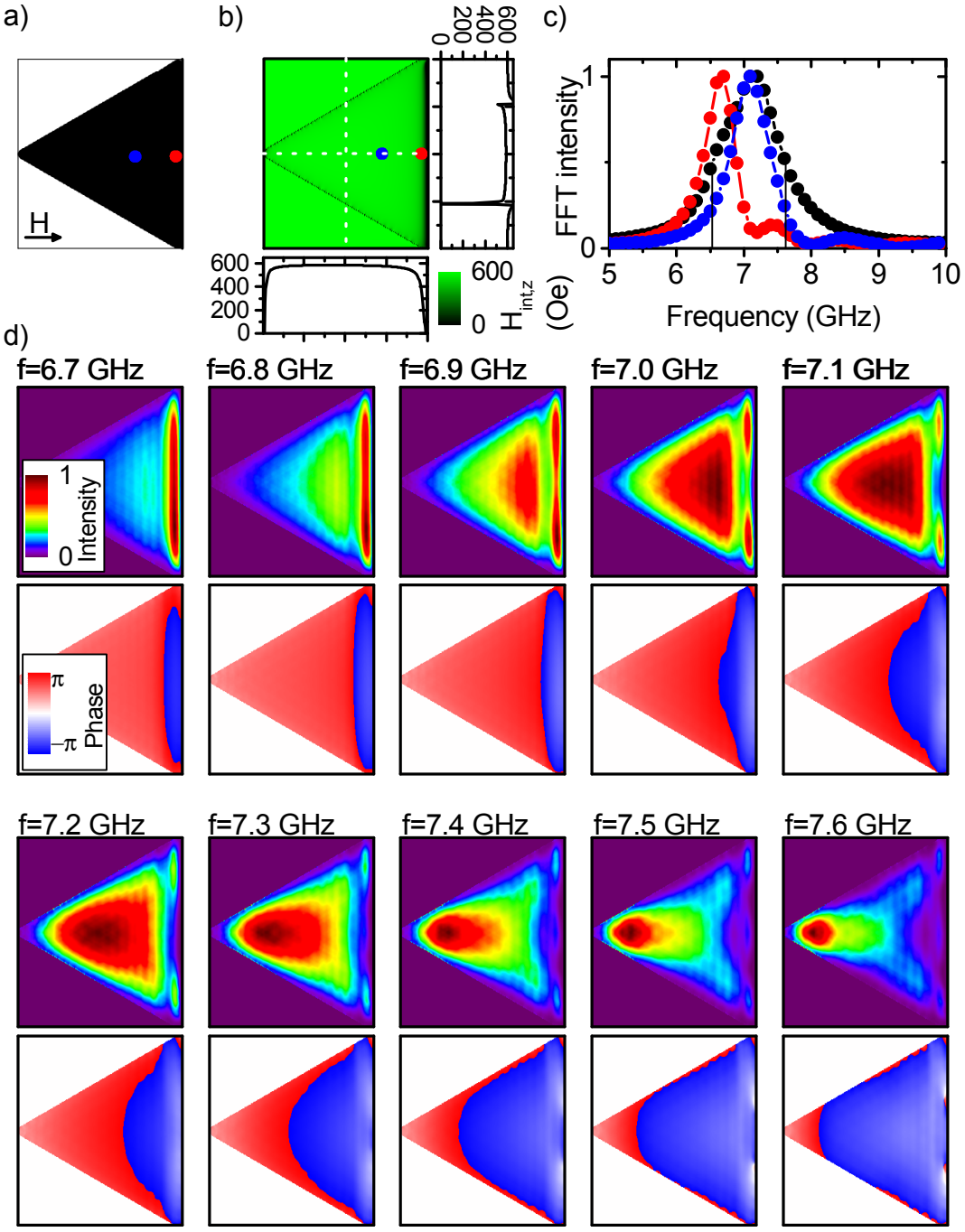

Figure 4.12: Spectrum of the Py triangle. a) Sketch of the model. Coloured dots indicate the points where spectra were extracted. **b)** Pseudocolour map of the z-component of the internal field H_{int}. Dotted lines correspond to the cross sections shown in the line plots. **c)** Spectrum averaged over all simulation cells (black) and acquired at the points indicated in a). **d)** Intensity and phase maps at frequencies ranging from $f = 6.7\,\mathrm{GHz}$ to $f = 7.6\,\mathrm{GHz}$.

from a local variation of the system parameters at the edge. First, the thickness of the sample is not a step-like function - it is however modelled as such in the simulation. The modelling of a decrease in thickness is difficult, because it would require a discretization of the sample along the x-direction and significantly increase computation time. Second, an imperfect element shape can have a large influence. Here, experimental imaging of the sample is necessary to model the sample correctly [93,110]. Third, magnetic moments at the surface clearly have a different environment compared to magnetic moments in the center. This can lead to surface or edge anisotropies, which critically depend on the boundary conditions imposed in the simulation [48, 84, 93]. Fourth, the fabrication of the sample can also lead to a change of the chemical composition at the edge, e.g. an oxidation. This in turn may influence magnetic parameters such as saturation magnetization M_S or Gilbert damping α_G [93].

In our case no experimental data was available. As a guess we therefore adjusted the saturation magnetization M_S of the sample at the base. A physically correct implementation of such an effect would require the adjustment of M_S at all three edges, but this is not possible using MuMax3.

The saturation magnetization was only changed in direction of the field as shown in Figure 4.13a. Instead of a sharp edge M_S decreases with an arctan profile from 800 G to 0 G. The influence on the internal field is small with deviations only close to the base (Figure 4.13b). The integrated spectrum in Figure 4.13c shows two changes:

- The center mode peak decreases to 7.0 GHz.
- An edge mode peak appears at 5.9 GHz. This is to be expected from the dispersion relation Equation 2.12 according to which a lower saturation magnetization corresponds to a lower frequency. The profiles at the edge and mode frequencies in Figure 4.13d show only slight changes compared to the sharp M_S edge.

Although this model fits better to the experimental data than the sharp edge model, agreement of the edge mode frequency is still not very good. We stress that for the quantitatively correct modelling of the edge modes independent experimental data is needed to characterise correctly the edges of the sample. Possible methods are scanning electron microscopy or scanning probe techniques such as magnetic force microscopy [112].

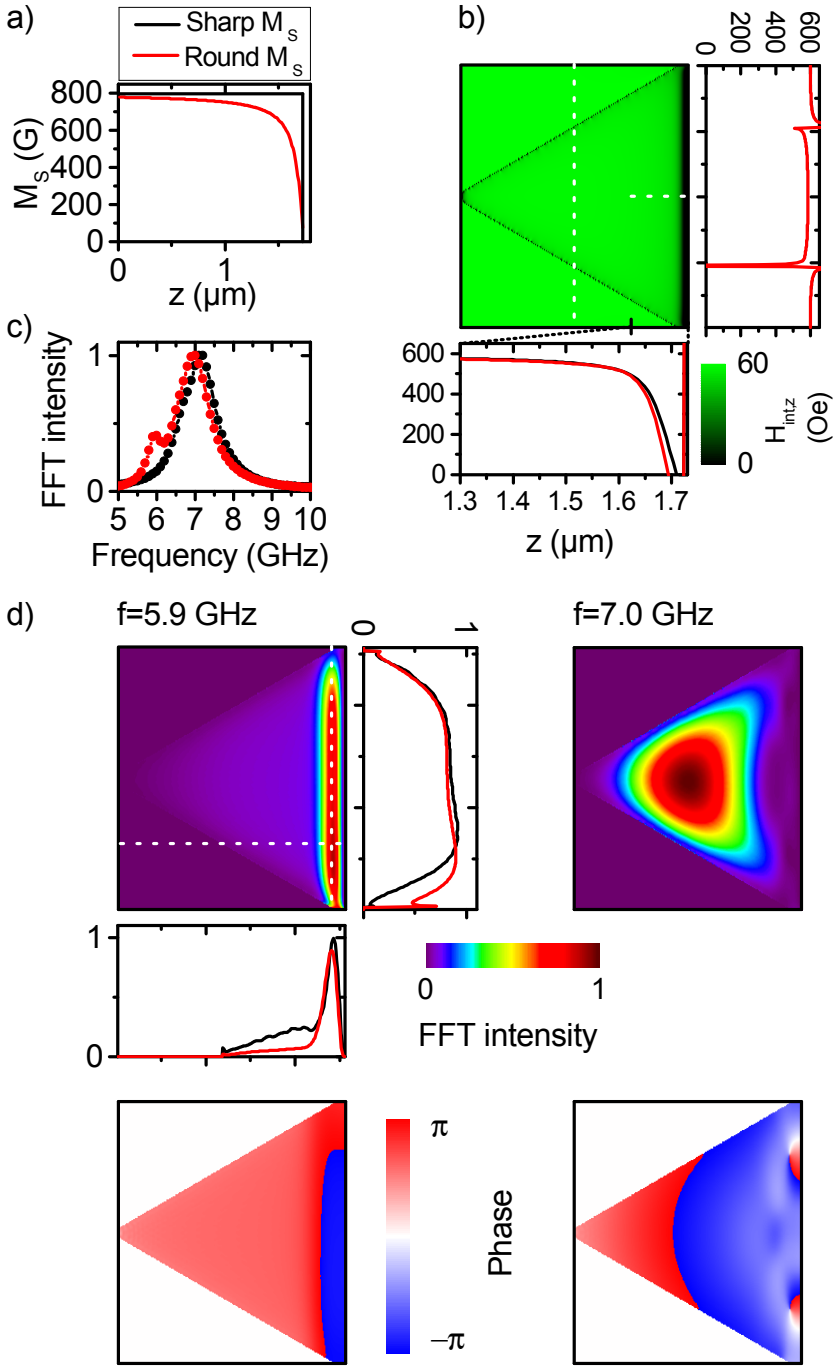

Figure 4.13: Effect of lowering M_S at the edge. a) Profile of the saturation magnetization M_S along the z-direction for the two models: sharp edge (black) and round edge (red). Corresponding **b)** internal field and **c)** spectrum averaged over all simulation cells. **d)** Intensity and phase maps at $f = 5.9\,\mathrm{GHz}$ and $f = 7.0\,\mathrm{GHz}$. Dotted lines correspond to the cross sections shown in the line plots.

4.2.2 Effect of the spin current

We analyse the behaviour of different spin waves modes under the influence of a spin transfer torque. Again, we start with a simple model, which is gradually adjusted to the experimental situation.

Single-mode excitation in the rectangle

One of the advantages of micromagnetic simulations is that it allows one to do *ceteris paribus* like experiments. One parameter of the system is changed while all others are kept constant. Clearly this is not possible in experiments, because for example the change of a magnetic parameter requires a new material - which in general, however, will also change other parameters.

Here, we have started our analysis by looking at the influence of the saturation magnetization, the mode frequency and the excitation amplitude on the fundamental mode in the rectangle (model 2).

The fundamental mode frequency as a function of saturation magnetization is shown in Figure 4.14a. The red line corresponds to the thin film dispersion relation Equation 2.12. Here, the wave vector was given by $k = \sqrt{k_z^2 + k_y^2}$ with $k_z = \pi/l_z$ and $k_y = \pi/l_y$ as well as $\varphi = \arctan(k_y/k_z)$. We see excellent agreement.

The dynamics of the spin transfer torque induced dynamics are analysed for charge currents ranging from 0 to 20 mA. The mode power was extracted at the center of the rectangle. As expected we see a non-linear growth of the power for larger currents. The inverse power, however, does not show the linear behaviour of Equation 2.32 but is slightly convex instead as indicated by the dotted lines. We see that the inverse power decreases faster for smaller saturation magnetization which is in agreement with Equation 2.31. This can also be directly inferred from the expression for the Slonczewski torque.

However, as a smaller M_S also leads to a smaller frequency it is not clear what the main influence is: the saturation magnetization or the frequency? To differentiate between those two effects we kept M_S fixed and changed the external field to match the four frequencies corresponding to the four different values of saturation magnetization. Figure 4.14c then shows that the frequency only has a small effect on the decrease of the inverse power. Hence, it is not possible to explain large differences in inverse power solely by frequency differences.

The center mode was excited using an rf magnetic field (see Section 3.2.1). The influence of the excitation amplitude $h_\sim$ was investigated for $M_S = 700\,\mathrm{G}$ for amplitudes ranging from 1 to 100 mOe. Due to the linear relationship between the amplitude of excitation and the amplitude of the dynamic magnetization [44, p. 14] we expect a quadratic dependence between the excitation amplitude and the absolute mode power. This was indeed observed as shown in Figure 4.14d and shows the validity of our approach of measuring the mode power. When looking at the relative power (as is always done in the inverse power plot) we see no dependence on the

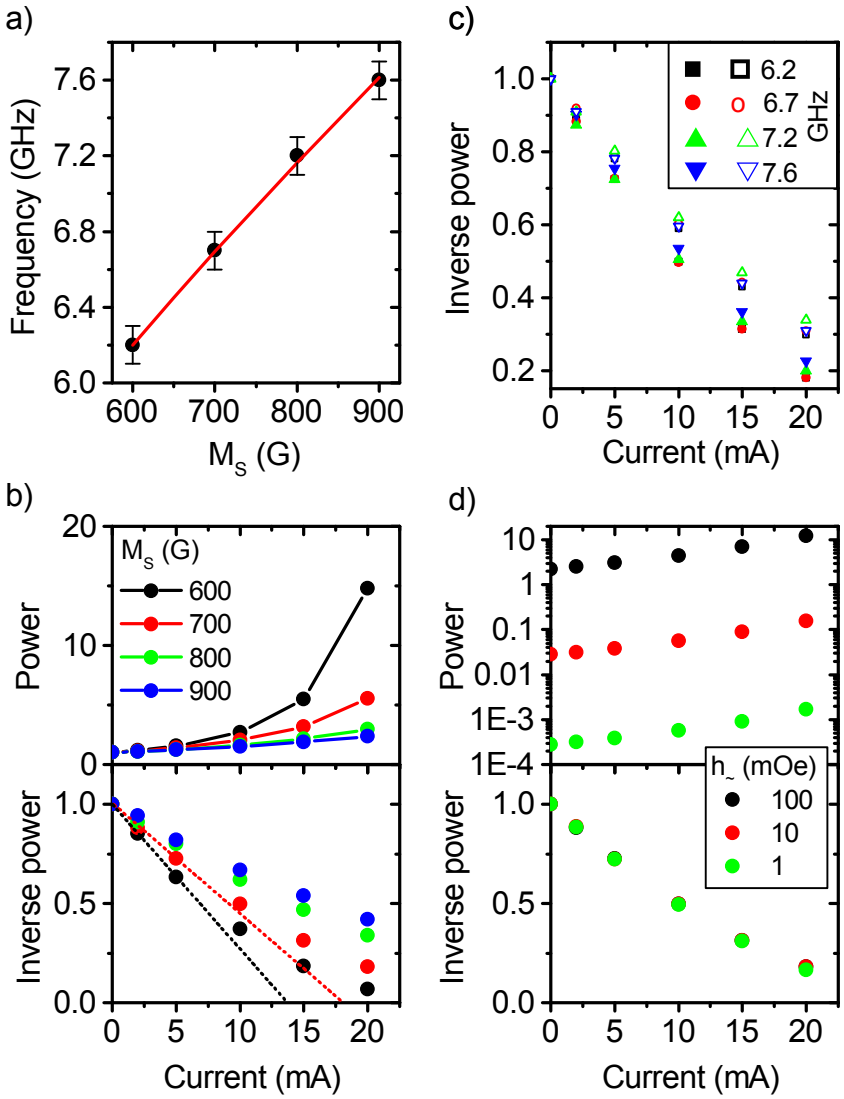

Figure 4.14: Dependence on saturation magnetization, frequency and excitation amplitude. a) Center mode frequency as a function of saturation magnetization M_S. Red line shows theoretical expectation based on the spin wave dispersion for a thin film. **b)** Effect of the spin current for different M_S: power (top) and normalised inverse power (bottom). Dotted lines are guide to the eye. **c)** Normalised inverse power for different frequencies and $M_S = 800\,\mathrm{G}$ (open symbols) and $M_S = 700\,\mathrm{G}$ (solid symbols). **d)** Power (top) and normalised inverse power (bottom) for different magnitudes of the excitation amplitude $h_\sim$.

excitation amplitude at all. In the following we have used an amplitude of 100 mOe.

We now analyse the spatial dependence of the influence of the spin current. Figure 4.15a shows the investigation scheme. The mode power is extracted at three different positions marked by coloured dots. The corresponding inverse power dependence in Figure 4.16b shows a clear picture: The inverse power decreases faster in the center compared to the edge. For $I = 20\,\mathrm{mA}$ the relative difference is more than 100 %. At the intermediate position an intermediate behaviour is seen. Also, the shape of the inverse power changes: It is convex at the center, nearly linear at the intermediate position and concave at the edge.

The spatially non-uniform behaviour corresponds to a change of the spatial profile of the mode power. This is shown in the two-dimensional maps in Figure 4.16c. For comparison the dotted blue lines in the cross sections show a profile

$$p = \cos^2\left(\frac{\pi}{l_{z,y}} r_{z,y}\right). \tag{4.7}$$

Along y the mode power profile does not change much in this current range. Along the field direction, for increasing current the mode power approaches the $\cos^2$ profile. For $I = 0\,\mathrm{mA}$ the profile is wider than the $\cos^2$ profile whereas at $I = 20\,\mathrm{mA}$ we see a good match. Hence, the mode power grows strongest at the position where it has its maximum for zero current. It does not grow at all where it was zero for zero current, for example at the boundaries. Put in more general terms, the mode power growth at a position depends on the relative strength of the mode at this position for zero current. It does not, however, depend on the absolute strength (see Figure 4.14d).

The same behaviour is seen for the edge mode in Figure 4.16. At the edge, where the initial mode power is large, the decrease of the inverse power is large. At the center, where the mode power is small, the decrease is small. The spatial profile of the edge mode power is shown in Figure 4.16c for $I = 0\,\mathrm{mA}$ and $I = 20\,\mathrm{mA}$. The peak in the profile also becomes more pronounced with larger current, but this is less visible compared to the center mode.

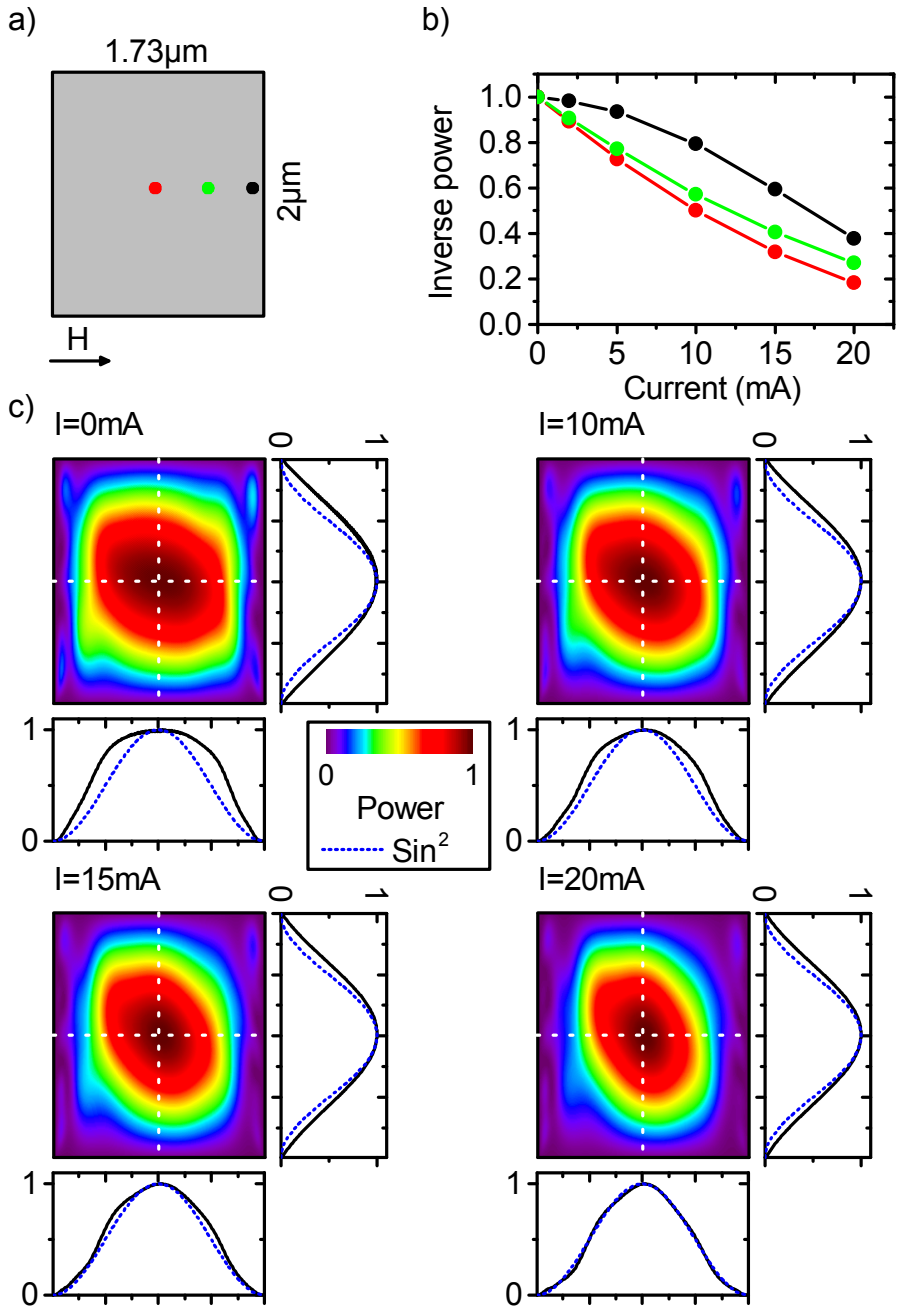

Figure 4.15: Dependence on position for the center mode. a) Model indicating the points where the mode power was measured. **b)** Normalised inverse mode power as a function of current at the positions indicated by the coloured dots in a). **c)** Maps of the mode power across the rectangle for different currents. White dotted lines correspond to the cross sections shown in the line plots. Blue dotted lines show $\cos^2$ function reaching from one end of the triangle to the other.

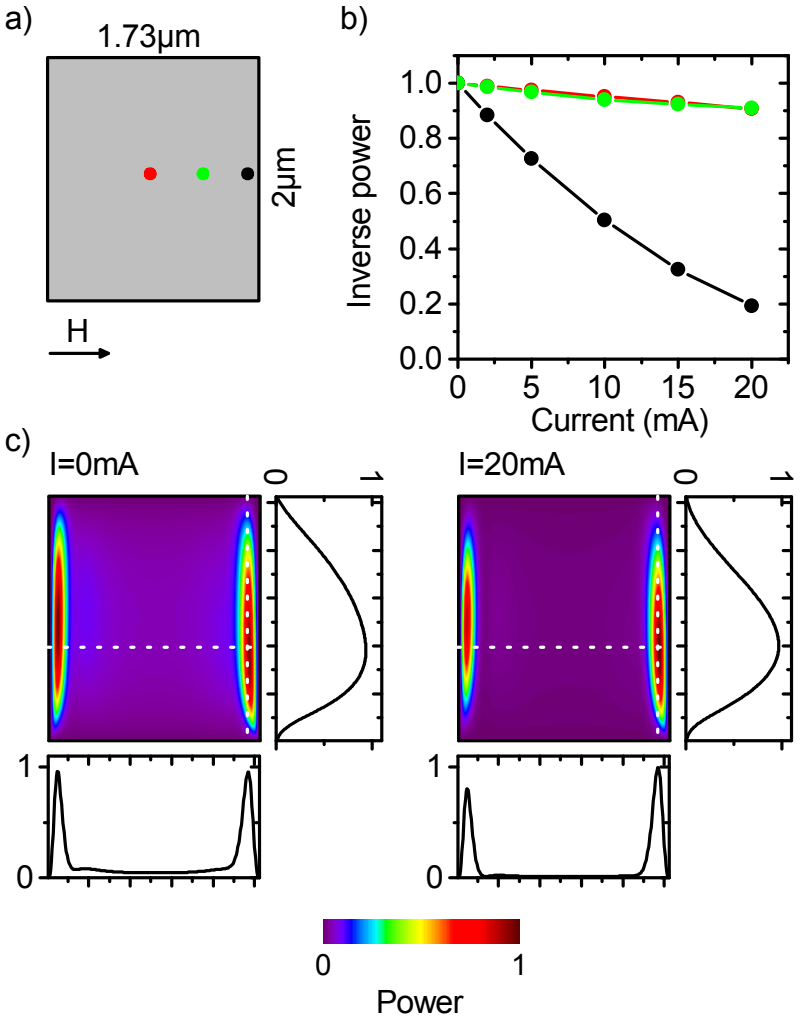

Figure 4.16: Dependence on position for the edge mode. a) Model indicating the points where the mode power was measured. **b)** Normalised inverse mode power as a function of current at the positions indicated by the coloured dots in a). **c)** Maps of the mode power across the rectangle for different currents. White dotted lines correspond to the cross sections shown in the line plots.

Multi-mode excitation in the rectangle

In this Section we compare the growth behaviour of the edge and the center mode power as function of position. Again we extracted the mode power at three different positions across the rectangle marked (1)-(3) in Figure 4.17.

For auto-oscillations above the threshold current $I > I_{\mathrm{th}}$ theory predicts that only one spin wave mode should survive in the steady state [38, 39]. The origin of this effect is that the two modes compete for the same energy source, namely the spin current. In our simulations we have compared the excitation of only one mode and of the edge and center mode simultaneously (Figure 4.17c and d). We do not find any difference between the two scenarios and the two modes seem to be completely independent.

Therefore, we expect the results of the previous Section to be valid for simultaneous excitation as well and indeed this is the case. Figure 4.17e shows that the center mode's inverse power decreases stronger at the center compared to the edge mode and vice versa at the edge. At position (2) both modes show a similar behaviour and the inverse power decreases linearly there.

As mentioned before the non-linear decrease of the inverse power is not in accordance with Equation (2.32). However, the underlying theory assumes that a spin wave mode can be described by a complex amplitude c. In principle, this does not limit the theory to uniform modes, but it does require that the spatial profile of the mode does not change as a function of current. As this is not the case in our simulations (Figures 4.15-4.17) the theory is no longer valid. We expect some agreement when averaging the power over the whole sample and indeed we then recover a linear dependence of the inverse power for a wider current range as presented in Figure 4.17e.

Multi-mode excitation in the triangle

The results obtained in the rectangle (model 2) are now tested for triangular geometry (model 3). Here, we found a quasi-continuous spin wave spectrum (Section 4.2.1). To investigate the influence of the spin current we excited the system at $f = 7.2\,\mathrm{GHz}$ and $f = 6.7\,\mathrm{GHz}$, corresponding to a peak mode power at the center and at the edge, respectively. For simplicity we refer to them as center and edge mode.

The spatial development of the mode power is shown in Figure 4.18. Both modes show a change in the spatial profile, mostly visible along the field direction. At $I = 0\,\mathrm{mA}$ the center mode occupies a large fraction of the triangle. With increasing current the peak near the center of the triangle becomes more pronounced and also shifts slightly towards the base of the triangle. At $I = 20\,\mathrm{mA}$ the mode occupies a much smaller area. This behaviour is consistent with experimental spatial maps of the center modes, which also showed the appearance of a more pronounced peak with increasing current.

The edge mode power shows a peak at the base and decays linearly towards the

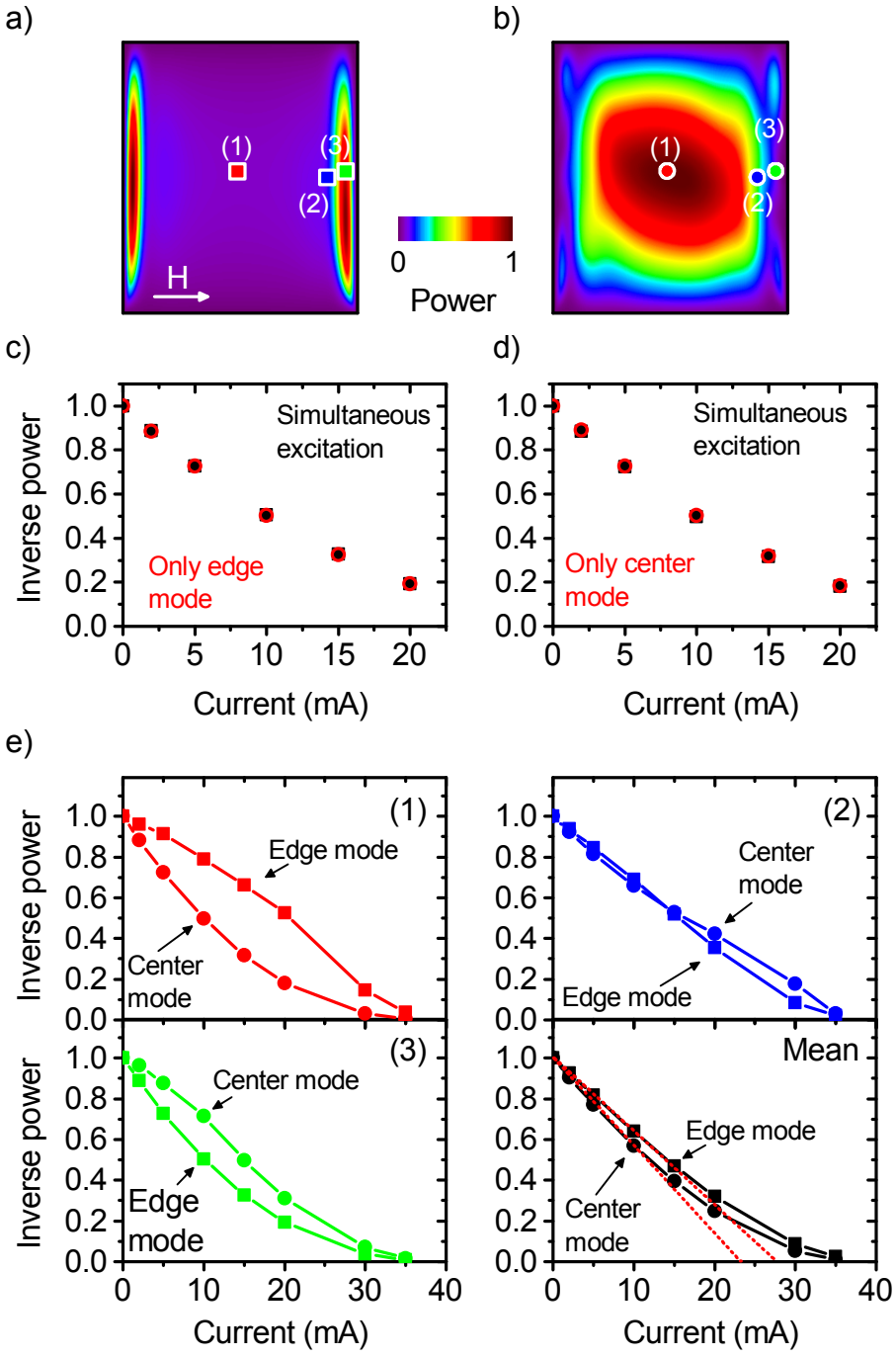

Figure 4.17: Comparison of edge and center mode enhanced by spin current. a) and b) Power maps for the edge (left) and center (right) mode at $I = 0\,\mathrm{mA}$. **c)** Normalised inverse power comparing the excitation of only one mode (red open circles) and both modes simultaneously (black squares). Left plot shows dependence for the edge mode where the power was extracted at position (3) in a). Right plot shows dependence for the center mode where the power was extracted at position (1). **e)** Normalised inverse power of the edge and center mode extracted at positions (1), (2) and (3) as indicated in a) and b). Black lines show normalised inverse power averaged over all simulation cells.

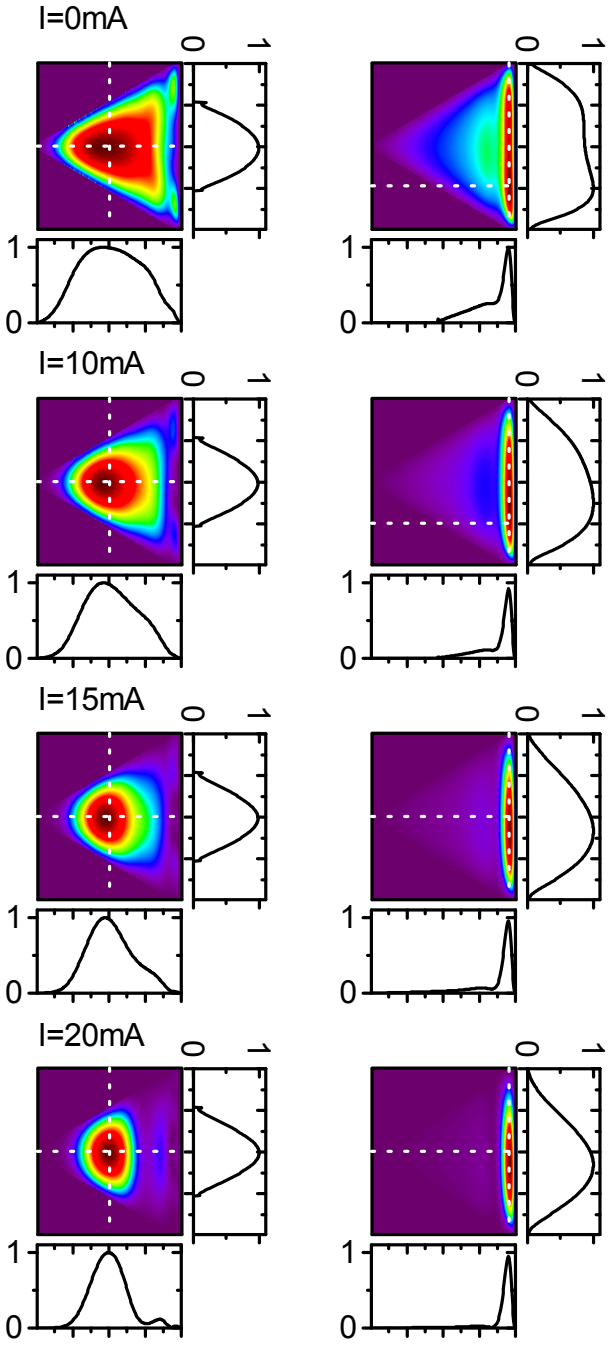

Figure 4.18: Mode power across the triangle. Mode power of the excitation at $f = 7.2\,\mathrm{GHz}$ (left) and at $f = 6.7\,\mathrm{GHz}$ (right) mode for different currents I. Dotted lines correspond to the cross sections shown in the line plots.

center of the triangle. With increasing current this decay becomes less visible and at $I = 20\,\mathrm{mA}$ the edge mode shows the profile of the edge mode in the rectangle. In y-direction, that means perpendicular to the external field, the mode profiles changes as well. At $I = 0\,\mathrm{mA}$ a dip is seen in the middle. This dip gradually transforms into a peak for increasing current. This is also seen in the experiment.

Figure 4.18 shows that we are able to qualitatively reproduce using micromagnetic simulation the spatial changes in the mode profiles seen in the experiment (Figure 4.3).

The mode growth in terms of the inverse power as a function of position is analysed in Figure 4.19. We extracted the inverse power at three different positions. At position (1) at the center the center mode's inverse power decreases much faster compared to the edge mode. At the edge, position (3), the opposite is seen. At position (2) both modes show nearly the same behaviour. Interestingly, for $I = 25\,\mathrm{mA}$ the gap between the two modes is closed, regardless of the position.

Figure 4.19 shows that the conclusions made for the rectangle are also valid in the triangular geometry: The influence of the spin-current on a spin wave mode is spatially non-uniform. The mode absorbs more energy in regions where it is also strong without any current applied. This is a remarkable result, because the current distribution is spatially uniform. Non-linear auto-oscillator theory fails in this case, because it requires a spatial profile of the spin wave, which does not change with increasing current [38].

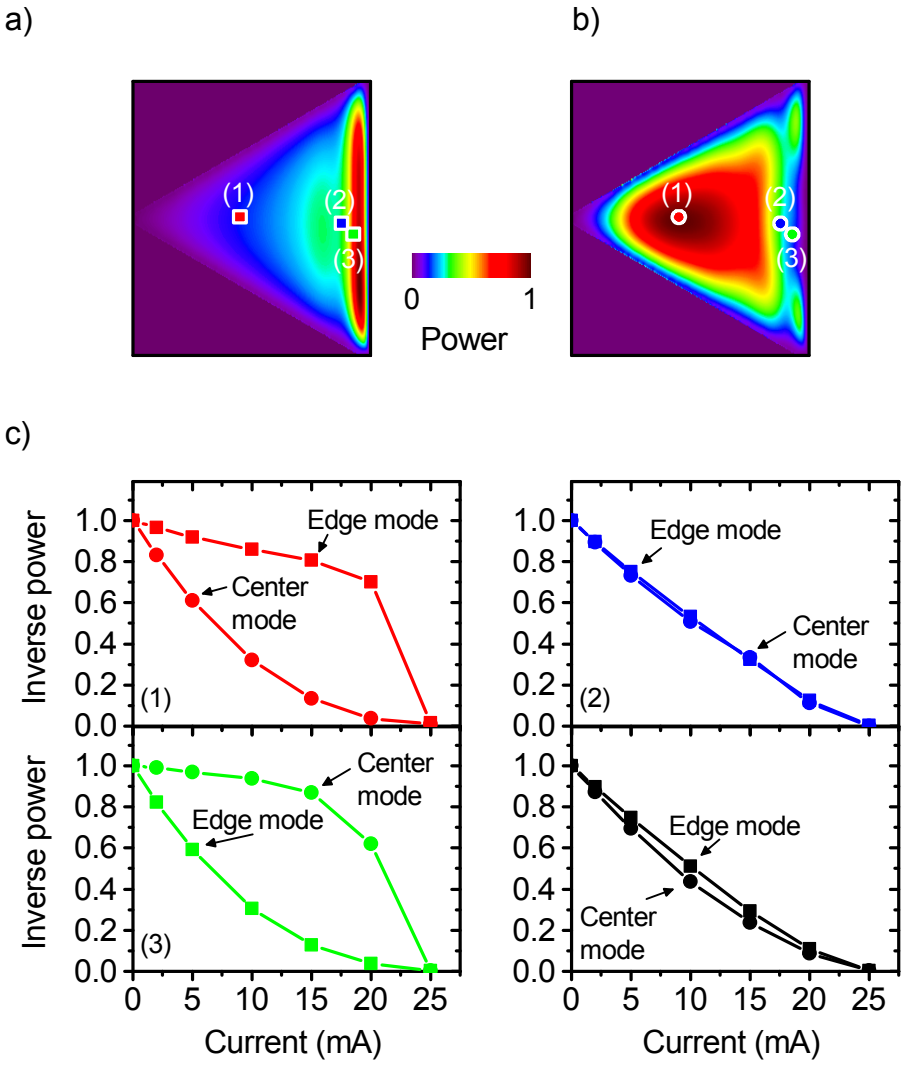

Figure 4.19: Comparison of edge and center mode in the triangle. a) and b) Power maps for the edge (left) and center (right) mode at $I = 0\,\mathrm{mA}$. **c)** Normalised inverse power of the edge and center mode extracted at positions (1), (2) and (3) as indicated in a) and b). Black lines show normalised inverse power averaged over all simulation cells.

Power efficient mode enhancement

We use the result of the spatially non-uniform mode enhancement for two applications. First, we show using micromagnetic simulation that local spin injection can be used for the power efficient enhancement of a mode. Second, we demonstrate that the local injection geometry can be used to selectively excite certain modes.

From the previous Sections we know that modes are most efficiently enhanced in areas where their zero current intensity is large. We use this for this for the power efficient enhancement of the edge mode in the triangle (model 3). The basic idea is that the effect of the spin current depends on the current *density* whereas the power consumption of some device is given by the current itself ($P = IU$). Therefore, we can increase the power efficiency by restricting the spin current injection to the area of large mode intensity as shown by the dotted lines in Figure 4.20.

We can then reach the same mode power (in absolute and relative terms) with only a tenth of the current (Figure 4.20a). In terms of current density we see in Figure 4.20b that the local excitation is slightly less efficient. The reason for this is that now radiation losses towards the center of the triangle have to be taken into account [29, 113–115]. Nevertheless the overall efficiency is about ten times higher compared to a non-local spin current injection.

Selective mode excitation

It is known that the shape of inductive (stripline) spin wave antennae can be patterned to optimise the excitation of spin waves [116]. In a similar way it is possible to pattern the spin current injection area to allow for the mode selective excitation of spin waves, as we show by means of micromagnetic simulation in Figure 4.21. We use the eigenmodes of model 1 for the demonstration.

To prepare the initial state we applied an rf magnetic field in such a way that the modes at $f = 9.5\,\mathrm{GHz}$ and $f = 11.5\,\mathrm{GHz}$ are excited with the same intensity. This is shown in the spectra at $I = 0\,\mathrm{mA}$. Then we apply the current.

With stripe 1 we apply the current in the region where the fundamental mode has its maximum and the higher order mode has a minimum. The result is shown on the left side of the Figure. Clearly the fundamental mode is selectively excited and dominates the spectrum for the whole current range up to $1.2\,\mathrm{mA}$.

On the other hand, the higher order mode can be selectively excited by injecting the current in the area where this mode has its maximum as is the case for the antenna stripes 2. In the spectra on the right the selective excitation can be clearly seen.

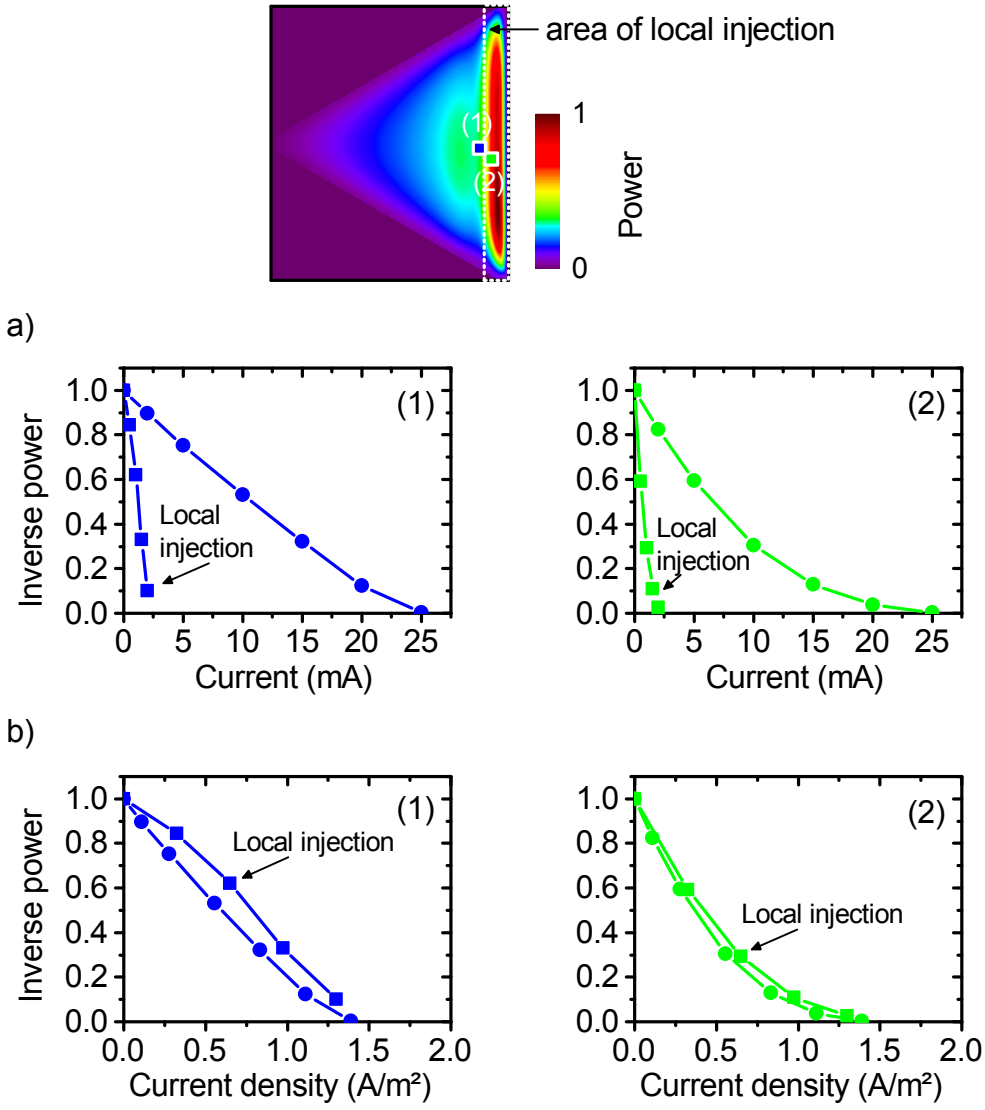

Figure 4.20: Local injection of spin current for efficient mode excitation. Map shows the edge mode power at $I = 0\,\mathrm{mA}$. Dotted rectangle indicates the area of local spin current injection. **a)** Normalised inverse power of the edge mode as a function of current measured at positions (1) and (2) as indicated in the map. Dots correspond to the non-local spin current injection across the whole of the triangle. Squares correspond to local injection. **b)** Normalised inverse power of the edge mode as a function of current *density* measured at positions (1) and (2) as indicated in the map.

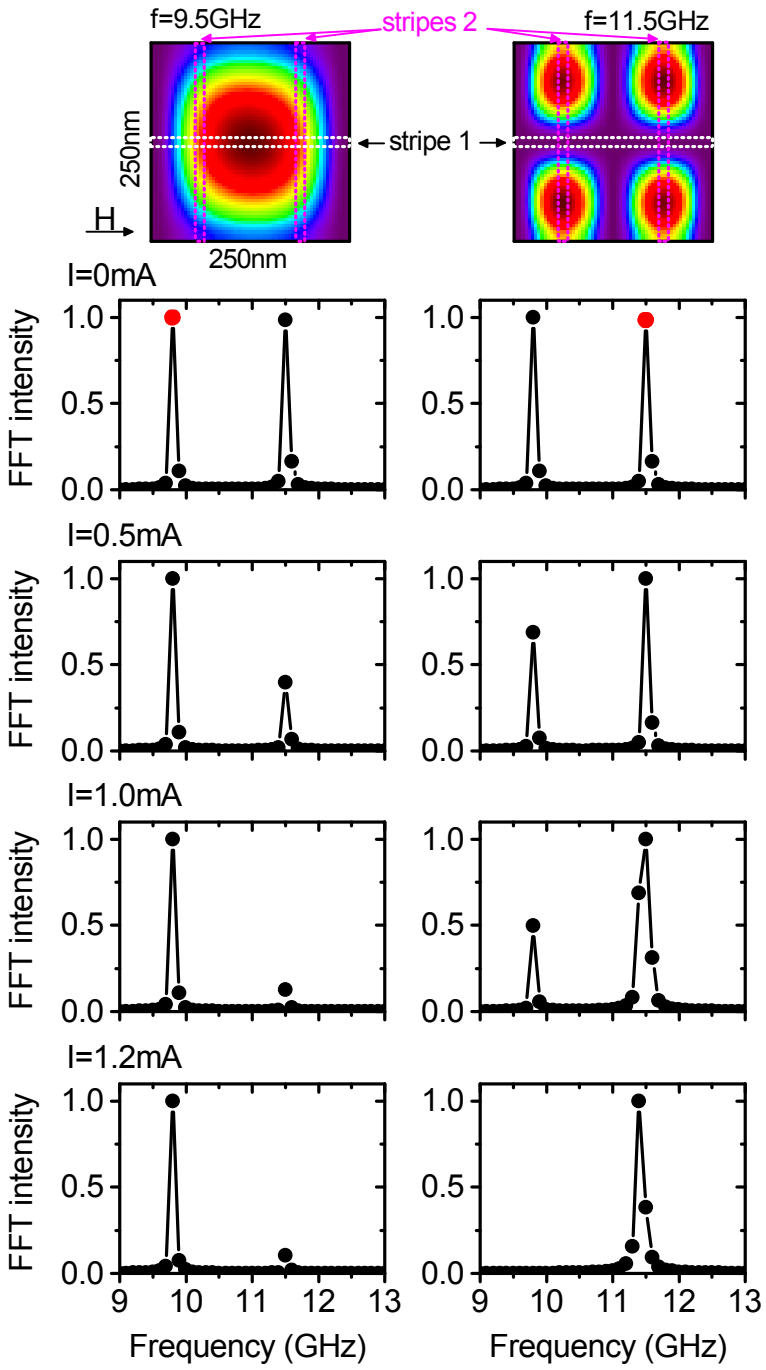

Figure 4.21: Mode selective excitation of spin waves. The dotted lines show the local spin injection geometries marked with stripe 1 and stripes 2. Stripe 1 leads to the selective excitation of the mode at 9.5 GHz (spectra on the left) whereas the stripes 2 selectively enhance the mode at 11.5 GHz (spectra on the right).

5 Conclusions

The aim of this thesis was the investigation of a multi-mode spin wave system subjected to a pure spin current. By means of microfocus Brillouin light scattering (microBLS) and micromagnetic simulation we have analysed how a spin current affects the spin wave modes in a Permalloy triangle. Here, we compare the results of the experiment and the simulation and point out possibilities for future investigations.

Spin wave spectrum in a triangle

The spin wave spectrum in an equilateral triangle with a side length of 2 µm showed at quasi-continuous spectrum, both in the experiment and the simulation. The frequencies of the modes increased from the base towards the apex of the triangle due to an increasing internal field and a decreasing localization length perpendicular to the field direction. The spatial profile of the modes evolved from the typical edge mode structure also seen in rectangles to center modes with an occupation of a large area within the triangle and finally corner modes at the apex of the triangle. Due to the low symmetry of the triangle subjected to a static field - only mirror symmetry with respect to the field direction is given - the modes cannot be approximated by eigenfunctions of the rectangular or the triangular geometry. Our results agree reasonably well with other investigations in triangles with smaller lateral dimensions [106, 111].

The quantitative agreement between spin wave frequencies in experiment and simulation was good for center modes without any adjustments of the typical material parameters for Permalloy. However, the edge modes showed quite large discrepancy of more than 1 GHz. We discussed possible reasons for this disagreement in Section 4.2.1. Here, we stress once more that the correct description of edge modes in micromagnetic simulation requires detailed information about the sample parameters: thickness, exact shape, edge roughness, rounding of the edges etc. Such information is a pre-requisite for successful modelling of edge modes and should be determined experimentally in future studies.

Effect of the spin current

Subjected to a pure spin current the multi-mode system showed two remarkable effects.

First, experiment and simulation showed that more than one spin wave mode - most probably even a multitude of modes - can be excited by spin current simultaneously.

This is contrary to theoretical expectations, which, however, mainly discuss the auto-oscillation behaviour above the threshold current whereas we have looked at the regime below the threshold [38,39]. For $I < I_{th}$ the modes can be excited independent of each other and no competing for the same energy source is observed. We also found no evidence for mode hopping in the simulation [40, 41]. In the experiment mode hopping on a sub-nanosecond time scale cannot be observed anyway due to the time integrating character of the measurement.

Second, the spatial profiles of the spin wave modes changed with increasing current. That means that a spatially uniform spin current enhances spin waves in a spatially non-uniform way. As a consequence of the non-uniformity we believe that non-linear auto-oscillator theory is no longer applicable [38]. The change in spatial profiles was seen in both BLS measurements (Figure 4.3) and spatial power maps from simulations (Figure 4.18). The modes absorb more energy in regions where they are also strong without any current applied. In the experiment this was most obvious at the edge of the sample where the edge mode intensity grew faster in a wide current range. Qualitatively the same behaviour is seen in the simulations.

Nevertheless, a direct comparison of experiment and simulation is difficult. Most importantly, the "initial" state without any current applied is different. Whereas in the simulation two distinct frequencies were excited by an rf magnetic field, in the experiment many spin wave modes were present according to Bose-Einstein statistics. Although it is in principle possible to include thermal fluctuations into the simulation, this did not prove to be a promising approach during the course of this project. Usually some low-threshold domain wall motion was excited, which absorbed all the energy and prevented the analysis of spin wave modes [117, 118]. The excitation by the rf magnetic field in the simulations also prevented the investigation of the frequency shift seen in the experiment.

The excitation of many modes in the experiment made it impossible to compare the behaviour of *single* modes. For example, when shifting the BLS laser spot from the base towards the center the spectrum already shifted upwards by 0.1 GHz indicating that at this position other modes were probed (in accordance with the increase of the frequency from the base to the apex).

In general, it turned out that the triangular geometry was not very well suited for the separate analysis of edge and center modes. This was mainly due to the quasi-continuous spectrum caused by the low symmetry of the structure and its large lateral size compared to the decay length as well as small thickness. In future experiment one should choose a geometry with rather well separated modes. We suggest a rectangular sample with a thickness of 10-20 nm and lateral dimensions of about 1 µm. Then one could expect a well known eigenmode spectrum described by cos-like magnetization profiles in the center and rather simple edge mode profiles. To reduce the influence of thermal noise at zero current one could also address single modes using parametric excitation first and then investigate the influence of the spin current [27, 119, 120].

Using non-local spin current injection geometries single-mode auto-oscillation of

the magnetization has been demonstrated. In this thesis we have shown using micromagnetic simulation that the spatially non-uniform enhancement of spin wave modes by spin current below the threshold of auto-oscillation can also be exploited using non-local spin injection geometries. In a simple model we have demonstrated the power efficient excitation of an edge mode and the selective excitation of one out of two modes in a Permalloy square. The controlled suppression and enhancement of spin wave modes might prove important on the road to novel magnonic devices.

Bibliography

[1] Roger Wood. Future hard disk drive systems. *Journal of Magnetism and Magnetic Materials*, 321(6):555–561, 2009.

[2] MN Baibich, JM Broto, A Fert, and FN Van Dau. Giant magnetoresistance of (001) Fe/(001) Cr magnetic superlattices. *Physical Review Letters*, 61(001):2472–2475, 1988.

[3] G Binasch, P Grünberg, F Saurenbach, and W Zinn. Enhanced magnetoresistance in layered magnetic structures with antiferromagnetic interlayer exchange. *Physical Review B*, 39(7):4828–4830, 1989.

[4] S. A. Wolf, D. D. Awschalom, R. A. Buhrman, J. M. Daughton, S. Von Molnár, M. L. Roukes, A. Y. Chtchelkanova, and D. M. Treger. Spintronics: a spin-based electronics vision for the future. *Science*, 294(5546):1488–95, November 2001.

[5] Igor Zutic, Jaroslav Fabian, and S Das Sarma. Spintronics: Fundamentals and applications. *Reviews of Modern Physics*, 76(2):323–410, 2004.

[6] V V Kruglyak, S O Demokritov, and D Grundler. Magnonics. *Journal of Physics D: Applied Physics*, 43(26):264001, July 2010.

[7] Sebastian Neusser and Dirk Grundler. Magnonics: Spin Waves on the Nanoscale. *Advanced Materials*, 21(28):2927–2932, July 2009.

[8] B. Lenk, H. Ulrichs, F. Garbs, and M. Münzenberg. The building blocks of magnonics. *Physics Reports*, 507(4-5):107–136, October 2011.

[9] Sergej O. Demokritov and AN Slavin. *Magnonics - From Fundamentals to Applications*. Springer, 1st edition, 2013.

[10] F Bloch. Zur Theorie des Ferromagnetismus. *Zeitschrift für Physik*, 61:206–219, 1930.

[11] RW Damon and H Van de Vaart. Dispersion of long-wavelength spin waves from pulse-echo experiments. *Physical Review Letters*, 12(21):583–585, 1964.

[12] Alexey V Kimel, Andrei Kirilyuk, Fredrik Hansteen, Roman V Pisarev, and Theo Rasing. Nonthermal optical control of magnetism and ultrafast laser-induced spin dynamics in solids. *Journal of Physics: Condensed Matter*, 19(4):043201, January 2007.

[13] M. Tsoi, a. Jansen, J. Bass, W.-C. Chiang, M. Seck, V. Tsoi, and P. Wyder. Excitation of a Magnetic Multilayer by an Electric Current. *Physical Review Letters*, 80(19):4281–4284, May 1998.

[14] E. B. Myers. Current-Induced Switching of Domains in Magnetic Multilayer Devices. *Science*, 285(5429):867–870, August 1999.

[15] SI Kiselev, JC Sankey, and IN Krivorotov. Microwave oscillations of a nanomagnet driven by a spin-polarized current. *Nature*, 425(September):380–383, 2003.

[16] S. Kaka, M. R. Pufall, W. H. Rippard, T. J. Silva, S. E. Russek, and J. a. Katine. Mutual phase-locking of microwave spin torque nano-oscillators. *Nature*, 437(September):389–392, 2005.

[17] K. Ando, S. Takahashi, K. Harii, K. Sasage, J. Ieda, S. Maekawa, and E. Saitoh. Electric Manipulation of Spin Relaxation Using the Spin Hall Effect. *Physical Review Letters*, 101(3):036601, July 2008.

[18] Tao Yang, Takashi Kimura, and Yoshichika Otani. Giant spin-accumulation signal and pure spin-current-induced reversible magnetization switching. *Nature Physics*, 4(11):851–854, October 2008.

[19] Luqiao Liu, Takahiro Moriyama, D. C. Ralph, and R. a. Buhrman. Spin-Torque Ferromagnetic Resonance Induced by the Spin Hall Effect. *Physical Review Letters*, 106(3):036601, January 2011.

[20] R. H. Liu, W. L. Lim, and S. Urazhdin. Spectral characteristics of the microwave emission by the spin Hall nano-oscillator. *Physical Review Letters*, 110(14):1–5, 2013.

[21] J. Hirsch. Spin Hall Effect. *Physical Review Letters*, 83(9):1834–1837, August 1999.

[22] Axel Hoffmann. Spin Hall Effects in Metals. *IEEE Transactions on Magnetics*, 49(10):5172–5193, October 2013.

[23] V. E. Demidov, S. Urazhdin, E. R. J. Edwards, and S. O. Demokritov. Wide-range control of ferromagnetic resonance by spin Hall effect. *Applied Physics Letters*, 99(17):172501, 2011.

[24] Zihui Wang, Yiyan Sun, Young Yeal Song, Mingzhong Wu, Helmut Schultheib, John E. Pearson, and Axel Hoffmann. Electric control of magnetization relaxation in thin film magnetic insulators. *Applied Physics Letters*, 99(16):97–100, 2011.

[25] E. Padrón-Hernández, a. Azevedo, and S. M. Rezende. Amplification of spin waves in yttrium iron garnet films through the spin Hall effect. *Applied Physics Letters*, 99(19), 2011.

[26] Shinya Kasai, Kouta Kondou, Hiroaki Sukegawa, Seiji Mitani, Kazuhito Tsukagoshi, and Yoshichika Otani. Modulation of effective damping constant using spin Hall effect. *Applied Physics Letters*, 104(9):2013–2016, 2014.

[27] E. R. J. Edwards, H. Ulrichs, V. E. Demidov, S. O. Demokritov, and S. Urazhdin. Parametric excitation of magnetization oscillations controlled by pure spin current. *Physical Review B*, 86(13):134420, October 2012.

[28] V. E. Demidov, S. Urazhdin, E. R. J. Edwards, M. D. Stiles, R. D. McMichael, and S. O. Demokritov. Control of Magnetic Fluctuations by Spin Current. *Physical Review Letters*, 107(10):107204, September 2011.

[29] Vladislav E Demidov, Sergei Urazhdin, Henning Ulrichs, Vasyl Tiberkevich, Andrei Slavin, Dietmar Baither, Guido Schmitz, and Sergej O Demokritov. Magnetic nano-oscillator driven by pure spin current. *Nature Materials*, 11(12):1028–31, December 2012.

[30] Luqiao Liu, Chi Feng Pai, D. C. Ralph, and R. a. Buhrman. Magnetic oscillations driven by the spin hall effect in 3-terminal magnetic tunnel junction devices. *Physical Review Letters*, 109(18):1–5, 2012.

[31] V. E. Demidov, S. Urazhdin, A. Zholud, A. V. Sadovnikov, and S. O. Demokritov. Nanoconstriction-based spin-Hall nano-oscillator. *Applied Physics Letters*, 105(17):172410, October 2014.

[32] H. Ulrichs, V. E. Demidov, and S. O. Demokritov. Micromagnetic study of auto-oscillation modes in spin-Hall nano-oscillators. *Applied Physics Letters*, 104(4):042407, January 2014.

[33] V E Demidov, H Ulrichs, S V Gurevich, S O Demokritov, V S Tiberkevich, a N Slavin, a Zholud, and S Urazhdin. Synchronization of spin Hall nano-oscillators to external microwave signals. *Nature communications*, 5:3179, January 2014.

[34] Zheng Duan, Andrew Smith, Liu Yang, Brian Youngblood, Jürgen Lindner, Vladislav E. Demidov, Sergej O. Demokritov, and Ilya N. Krivorotov. Nanowire spin torque oscillator driven by spin orbit torques. *Nature Communications*, 5:5616, 2014.

[35] V. E. Demidov, S. Urazhdin, a. Zholud, a. V. Sadovnikov, a. N. Slavin, and S. O. Demokritov. Spin-current nano-oscillator based on nonlocal spin injection. *Scientific Reports*, 5(8):8578, 2015.

[36] Sergej O Demokritov. *Spin wave confinement*. Pan Stanford Publishing, 2009.

[37] Vladislav E. Demidov, Sergej O. Demokritov, Karsten Rott, Patryk Krzysteczko, and Guenter Reiss. Nano-optics with spin waves at microwave frequencies. *Applied Physics Letters*, 92(23):2–5, 2008.

[38] Andrei Slavin and Vasil Tiberkevich. Nonlinear auto-oscillator theory of microwave generation by spin-polarized current. *Magnetics, IEEE Transactions on*, 45(4):1875–1918, 2009.

[39] F. M. De Aguiar, a. Azevedo, and S. M. Rezende. Theory of a two-mode spin torque nanooscillator. *Physical Review B - Condensed Matter and Materials Physics*, 75(13):1–4, 2007.

[40] P. K. Muduli, O. G. Heinonen, and Johan Å kerman. Decoherence and mode hopping in a magnetic tunnel junction based spin torque oscillator. *Physical Review Letters*, 108(20):1–5, 2012.

[41] Stefano Bonetti, Vasil Tiberkevich, Giancarlo Consolo, Giovanni Finocchio, Pranaba Muduli, Fred Mancoff, Andrei Slavin, and Johan Å kerman. Experimental evidence of self-localized and propagating spin wave modes in obliquely magnetized current-driven nanocontacts. *Physical Review Letters*, 105(21):1–4, 2010.

[42] P. K. Muduli, O. G. Heinonen, and Johan Å kerman. Temperature dependence of linewidth in nanocontact based spin torque oscillators: Effect of multiple oscillatory modes. *Physical Review B - Condensed Matter and Materials Physics*, 86(17):1–7, 2012.

[43] J. Stöhr and H. C. Siegmann. *Magnetism - From Fundamentals to Nanoscale Dynamics*. Springer Berlin Heidelberg, 2006.

[44] A. G. Gurevich and G. A. Melkov. *Magnetization Oscillations and Waves*. CRC Press, 1996.

[45] T.L. Gilbert. A Phenomenological Theory of Damping in Ferromagnetic Materials. *IEEE Transactions on Magnetics*, 40(6):3443–3449, 2004.

[46] Werner Heisenberg. Zur Theorie des Ferromagnetismus. *Zeitschrift Für Physik*, 49(9-10):619–636, 1928.

[47] GS Abo, YK Hong, and Jihoon Park. Definition of magnetic exchange length. *IEEE Transactions on Magnetics*, 49(8):4937–4939, 2013.

[48] Amikam Aharoni. *Introduction to the Theory of Ferromagnetism*. Oxford Science Publications, 2nd edition, 2006.

[49] C Kittel. On the theory of ferromagnetic resonance absorption. *Physical Review*, 460(1946), 1948.

[50] R.W. Damon and J.R. Eshbach. Magnetostatic modes of a ferromagnet slab. *Journal of Physics and Chemistry of Solids*, 19(3-4):308–320, 1961.

[51] BA Kalinikos and AN Slavin. Theory of dipole-exchange spin wave spectrum for ferromagnetic films with mixed exchange boundary conditions. *Journal of Physics C: Solid State Physics*, 7013, 1986.

[52] T. Wolfram and R.E. de Wames. Dipole-exchange modes of a thin ferromagnetic film, 1969.

[53] R. E. De Wames and T. Wolfram. Dipole-exchange spin waves in ferromagnetic films. *Journal of Applied Physics*, 41(3):987–993, 1970.

[54] G.T. Rado and J.R. Weertman. Spin-wave resonance in a ferromagnetic metal. *Journal of Physics and Chemistry of Solids*, 11(3-4):315–333, 1959.

[55] Daniel D. Stancil and Anil Prabhakar. *Spin Waves - Theory and Applications*. Springer, 2010.

[56] R. I. Joseph and E. Schlömann. Demagnetizing field in nonellipsoidal bodies. *Journal of Applied Physics*, 36(5):1579–1593, 1965.

[57] J Jorzick, S O Demokritov, B Hillebrands, M Bailleul, C Fermon, K Y Guslienko, a N Slavin, D V Berkov, and N L Gorn. Spin wave wells in nonellipsoidal micrometer size magnetic elements. *Physical review letters*, 88(4):047204, 2002.

[58] G. Gubbiotti, G. Carlotti, T. Okuno, M. Grimsditch, L. Giovannini, F. Montoncello, and F. Nizzoli. Spin dynamics in thin nanometric elliptical Permalloy dots: A Brillouin light scattering investigation as a function of dot eccentricity. *Physical Review B - Condensed Matter and Materials Physics*, 72(18):1–8, 2005.

[59] C. Bayer. Spin-Wave Excitations in Finite Rectangular Elements. In *Spin Dynamics in Confined Magnetic Structures III*. Springer, 2006.

[60] Christian Bayer, Jörg Jorzick, Sergej O. Demokritov, Andrei N. Slavin, Konstantin Y. Guslienko, Dmitry V. Berkov, Natalia L. Gorn, Mikhail P. Kostylev, and Burkard Hillebrands. Spin-wave excitations in finite rectangular elements. *Topics in Applied Physics*, 101:57–103, 2006.

[61] S.O. Demokritov and V. E. Demidov. Quantized Spin-Wave Modes Due To Lateral Confinement. In *Spin Wave Confinement*. Pan Stanford Publishing, 2009.

[62] Vasil Tiberkevich and Andrei Slavin. Nonlinear phenomenological model of magnetic dissipation for large precession angles: Generalization of the Gilbert model. *Physical Review B - Condensed Matter and Materials Physics*, 75(1):1–6, 2007.

[63] M. I. D. D'yakonov and V. I. Perel'. Possibilty of orienting electron spins with current. *Sov. Phys. JETP Lett.*, 13(11):467, 1971.

[64] J. Smit and J. Volger. Spontaneous Hall effect in ferromagnetics. *Physical Review*, 92(6):1576–1577, 1953.

[65] Z. Feng, J. Hu, L. Sun, B. You, D. Wu, J. Du, W. Zhang, a. Hu, Y. Yang, D. M. Tang, B. S. Zhang, and H. F. Ding. Spin Hall angle quantification from spin pumping and microwave photoresistance. *Physical Review B - Condensed Matter and Materials Physics*, 85(21):1–7, 2012.

[66] Matthias Althammer, Sibylle Meyer, Hiroyasu Nakayama, Michael Schreier, Stephan Altmannshofer, Mathias Weiler, Hans Huebl, Stephan Geprägs, Matthias Opel, Rudolf Gross, Daniel Meier, Christoph Klewe, Timo Kuschel, Jan Michael Schmalhorst, Günter Reiss, Liming Shen, Arunava Gupta, Yan Ting Chen, Gerrit E W Bauer, Eiji Saitoh, and Sebastian T B Goennenwein. Quantitative study of the spin Hall magnetoresistance in ferromagnetic insulator/normal metal hybrids. *Physical Review B - Condensed Matter and Materials Physics*, 87(22):1–15, 2013.

[67] M. D. Stiles and a. Zangwill. Anatomy of Spin-Transfer Torque. page 16, 2002.

[68] I N Krivorotov, N C Emley, J C Sankey, S I Kiselev, D C Ralph, and R a Buhrman. Time-domain measurements of nanomagnet dynamics driven by spin-transfer torques. *Science*, 307(5707):228–31, January 2005.

[69] J.C. Slonczewski. Current-driven excitation of magnetic multilayers. *Journal of Magnetism and Magnetic Materials*, 159:L1–L7, June 1996.

[70] L Berger. Emission of spin waves by a magnetic multilayer traversed by a current. *Physical Review B*, 54(13):9353–9358, 1996.

[71] J.C Slonczewski. Excitation of spin waves by an electric current. *Journal of Magnetism and Magnetic Materials*, 195(2):L261–L268, 1999.

[72] AN Slavin and Pavel Kabos. Approximate theory of microwave generation in a current-driven magnetic nanocontact magnetized in an arbitrary direction. *Magnetics, IEEE Transactions on*, 41(4):1264–1273, 2005.

[73] W H Rippard, M R Pufall, S Kaka, S E Russek, and T J Silva. Direct-current induced dynamics in Co90 Fe10/Ni80 Fe20 point contacts. *Physical review letters*, 92(2):027201, 2004.

[74] Vladislav E Demidov, Sergei Urazhdin, and Sergej O Demokritov. Direct observation and mapping of spin waves emitted by spin-torque nano-oscillators. *Nature materials*, 9(12):984–988, 2010.

[75] M. Madami, S. Bonetti, G. Consolo, S. Tacchi, G. Carlotti, G. Gubbiotti, F. B. Mancoff, M. a. Yar, and J. Å kerman. Direct observation of a propagating spin wave induced by spin-transfer torque. *Nature Nanotechnology*, 6(10):635–638, 2011.

[76] William Fuller Brown. Thermal Fluctuations of a Single-Domain Particle. *Journal of Applied Physics*, 34(4):1319, 1963.

[77] Henning Ulrichs. *Spin-wave instabilities on the nanoscale.* PhD thesis, Westfälische Wilhelms-Universität Münster, 2014.

[78] SO Demokritov, B Hillebrands, and AN Slavin. Brillouin light scattering studies of confined spin waves: linear and nonlinear confinement. *Physics Reports*, 348:441–489, 2001.

[79] J Jorzick, SO Demokritov, and C Mathieu. Brillouin light scattering from quantized spin waves in micron-size magnetic wires. *Physical Review B*, 60(22):194–200, 1999.

[80] S.O. Demokritov and V.E. Demidov. Micro-Brillouin Light Scattering Spectroscopy of Magnetic Nanostructures. *IEEE Transactions on Magnetics*, 44(1):6–12, January 2008.

[81] H. Ulrichs, V. E. Demidov, S. O. Demokritov, W. L. Lim, J. Melander, N. Ebrahim-Zadeh, and S. Urazhdin. Optimization of Pt-based spin-Hall-effect spintronic devices. *Applied Physics Letters*, 102(13):2–5, 2013.

[82] Sang-Koog Kim. Micromagnetic computer simulations of spin waves in nanometre-scale patterned magnetic elements. *Journal of Physics D: Applied Physics*, 43(26):264004, July 2010.

[83] Bruno Azzerboni, Giancarlo Consolo, and Giovanni Finocchio. Micromagnetic Modeling of Nanoscale Spin Valves. In Klaus D. Sattler, editor, *Handbook of Nanophysics: Nanoelectronics and Nanophotonics*. CRC Press, 2010.

[84] M. J. Donahue and D. G. Porter. Exchange energy formulations for 3D micromagnetics. *Physica B: Condensed Matter*, 343(1-4):177–183, 2004.

[85] M. Mansuripur and R. Giles. Demagnetizing field computation for dynamic simulation of the magnetization reversal process. *IEEE Transactions on Magnetics*, 24(6):2326–2328, 1988.

[86] Arne Vansteenkiste, Jonathan Leliaert, Mykola Dvornik, Mathias Helsen, Felipe Garcia-Sanchez, and Bartel Van Waeyenberge. The design and verification of MuMax3. *AIP Advances*, 4(10):107133, October 2014.

[87] L Lopez-Diaz, D Aurelio, L Torres, E Martinez, M a Hernandez-Lopez, J Gomez, O Alejos, M Carpentieri, G Finocchio, and G Consolo. Micromagnetic simulations using Graphics Processing Units. *Journal of Physics D: Applied Physics*, 45(32):323001, 2012.

[88] *Mathematica 9.0*. Wolfram Research, Champaign, Illinois, 2013.

[89] F. Boust and N. Vukadinovic. Micromagnetic simulations of vortex-state excitations in soft magnetic nanostructures. *Physical Review B - Condensed Matter and Materials Physics*, 70(17):1–4, 2004.

[90] a. Romeo, G. Finocchio, M. Carpentieri, L. Torres, G. Consolo, and B. Azzerboni. A numerical solution of the magnetization reversal modeling in a permalloy thin film using fifth order Runge-Kutta method with adaptive step size control. *Physica B: Condensed Matter*, 403(2-3):464–468, 2008.

[91] R. D. McMichael and M. D. Stiles. Magnetic normal modes of nanoelements. *Journal of Applied Physics*, 97(10), 2005.

[92] Claude E. Shannon. Communication In The Presence Of Noise. *Proceedings of the IEEE*, 86(2), 1998.

[93] D.V. Berkov and J. Miltat. Spin-torque driven magnetization dynamics: Micromagnetic modeling. *Journal of Magnetism and Magnetic Materials*, 320(7):1238–1259, April 2008.

[94] Soo-Man Seo, Kyoung-Whan Kim, Jisu Ryu, Hyun-Woo Lee, and Kyung-Jin Lee. Current-induced motion of a transverse magnetic domain wall in the presence of spin Hall effect. *Applied Physics Letters*, 101(2):022405, 2012.

[95] L. Thevenard, H. T. Zeng, D. Petit, and R. P. Cowburn. Six-fold configurational anisotropy and magnetic reversal in nanoscale Permalloy triangles. *Journal of Applied Physics*, 106(6):063902, 2009.

[96] Wai-Kee Li and S M Blinder. Solution of the Schrödinger equation for a particle in an equilateral triangle. *Journal Of Mathematical Physics*, 26(1):2784–2786, 1985.

[97] Wajdi Gaddah. A Lie group approach to the Schrödinger equation for a particle in an equilateral triangular infinite well. *European Journal of Physics*, 34(5):1175–1186, 2013.

[98] Marcin Wojdyr. Fityk: A general-purpose peak fitting program. *Journal of Applied Crystallography*, 43(5 PART 1):1126–1128, 2010.

[99] Philipp Seibt. Report for miniForschung, 2014.

[100] F. Sánchez-Bajo and F. L. Cumbrera. The use of the pseudo-Voigt function in the variance method of X-ray line-broadening analysis. *Journal of Applied Crystallography*, 30(5):550–550, 1997.

[101] Wolfgang Rave and Alex Hubert. Magnetic ground state of a thin-film element. *IEEE Transactions on Magnetics*, 36(6):3886–3899, 2000.

[102] Jian-Gang Zhu, Youfeng Zheng, and Xiangdong Lin. Micromagnetics of small size patterned exchange biased Permalloy film elements. *Journal of Applied Physics*, 81(8):4336, 1997.

[103] G. Gubbiotti, L. Albini, G. Carlotti, M. De Crescenzi, E. Di Fabrizio, a. Gerardino, O. Donzelli, F. Nizzoli, H. Koo, and R. D. Gomez. Finite size effects in patterned magnetic permalloy films. *Journal of Applied Physics*, 87(9):5633, 2000.

[104] V K Vlasko-Vlasov, E Palacious, D Rosenmann, J Pearson, Y Jia, Y L Wang, U Welp, and W-K Kwok. Self-healing patterns in ferromagnetic-superconducting hybrids. *Superconductor Science and Technology*, 28(3):035006, 2015.

[105] K. Guslienko, S. Demokritov, B. Hillebrands, and a. Slavin. Effective dipolar boundary conditions for dynamic magnetization in thin magnetic stripes. *Physical Review B*, 66(13):8–11, 2002.

[106] Federico Montoncello and Fabrizio Nizzoli. Spin modes of triangular magnetic nanodots in the vortex, Y, and buckle states. *Journal of Applied Physics*, 107(2):023906, 2010.

[107] H. Schultheiss, S. Schäfer, P. Candeloro, B. Leven, B. Hillebrands, and a. N. Slavin. Observation of coherence and partial decoherence of quantized spin waves in nanoscaled magnetic ring structures. *Physical Review Letters*, 100(4):2–5, 2008.

[108] B. B. Maranville, R. D. McMichael, S. a. Kim, W. L. Johnson, C. a. Ross, and Joy Y. Cheng. Characterization of magnetic properties at edges by edge-mode dynamics. *Journal of Applied Physics*, 99(8):2004–2007, 2006.

[109] V. V. Kruglyak, P. S. Keatley, R. J. Hicken, J. R. Childress, and J. a. Katine. Time resolved studies of edge modes in magnetic nanoelements. *Journal of Applied Physics*, 99(8), 2006.

[110] P. S. Keatley, P. Gangmei, M. Dvornik, R. J. Hicken, J. R. Childress, and J. a. Katine. Large amplitude magnetization dynamics and the suppression of edge modes in a single nanomagnet. *Applied Physics Letters*, 98(8):1–4, 2011.

[111] C. S. Lin, H. S. Lim, C. C. Wang, a. O. Adeyeye, Z. K. Wang, S. C. Ng, and M. H. Kuok. Spin wave localization in a triangular nanomagnet. *Journal of Applied Physics*, 108(11), 2010.

[112] Y. Martin and H. K. Wickramasinghe. Magnetic imaging by "force microscopy" with 1000 A resolution. *Applied Physics Letters*, 50(20):1455–1457, 1987.

[113] Giancarlo Consolo, Bruno Azzerboni, Grant Gerhart, Gennady a. Melkov, Vasil Tiberkevich, and Andrei N. Slavin. Excitation of self-localized spin-wave bullets by spin-polarized current in in-plane magnetized magnetic nanocontacts: A micromagnetic study. *Physical Review B - Condensed Matter and Materials Physics*, 76(14):1–8, 2007.

[114] G. Consolo. Spin-wave excitation by spin-polarized current in magnetic nanostructures. *Physica Status Solidi (C) Current Topics in Solid State Physics*, 5(7):2391–2395, 2008.

[115] S Urazhdin, V E Demidov, H Ulrichs, T Kendziorczyk, T Kuhn, J Leuthold, G Wilde, and S O Demokritov. Nanomagnonic devices based on the spin-transfer torque. *Nature nanotechnology*, 9(7):509–13, July 2014.

[116] V. Vlaminck and M. Bailleul. Spin-wave transduction at the submicrometer scale: Experiment and modeling. *Physical Review B - Condensed Matter and Materials Physics*, 81(1):1–13, 2010.

[117] Yoshinobu Nakatani, André Thiaville, and Jacques Miltat. Faster magnetic walls in rough wires. *Nature materials*, 2(8):521–3, August 2003.

[118] A. Thiaville, Y Nakatani, J. Miltat, and N. Vernier. Domain wall motion by spin-polarized current: a micromagnetic study. *Journal of Applied Physics*, 95(11):7049, 2004.

[119] Henning Ulrichs, Vladislav E. Demidov, Sergej O. Demokritov, and Sergei Urazhdin. Parametric excitation of eigenmodes in microscopic magnetic dots. *Physical Review B - Condensed Matter and Materials Physics*, 84(9):1–6, 2011.

[120] T. Brächer, P Pirro, B Obry, B Leven, AA Serga, and B Hillebrands. Mode selective parametric excitation of spin waves in a Ni81Fe19 microstripe. *Applied Physics Letters*, 99(16):162501, 2011.

Acknowledgment

Coming back from my study year abroad in London I was very much looking forward to the MSc project in Germany. As I had enjoyed my work for my BSc thesis in the work group of Prof Demokritov I was happy to return to my old office and I thank him for giving me the opportunity to do research in the field of magnonics, again.

I would also like to thank Henning Ulrichs, who is now at the University of Göttingen, for his supervision during the first weeks of the project, which made my start into the dynamics driven by pure spin current easier. For the rest of the year Vladislav E. Demidov always had an open ear and in times of problems helped to find the right approach again, for which I am very grateful to him.

Also, I thank Michael Evelt, my office neighbour, for fruitful discussions - about physics and about all the other more or less important things in life.

Finally, I thank my friends and family, who were always there with a cup of coffee, encouragement and - if needed - distraction.

Münster, May 2015 *Philipp Seibt*

Plagiatserklärung

Hiermit versichere ich, Philipp Seibt, dass die vorliegende Arbeit selbstständig verfasst worden ist, dass keine anderen Quellen und Hilfsmittel als die angegebenen benutzt worden sind und dass die Stellen der Arbeit, die anderen Werken - auch elektronischen Medien - dem Wortlaut oder Sinn nach entnommen wurden, auf jeden Fall unter Angabe der Quelle als Entlehnung kenntlich gemacht worden sind.

Ich erkläre mich mit einem Abgleich der Arbeit mit anderen Texten zwecks Auffindung von Übereinstimmungen sowie mit einer zu diesem Zweck vorzunehmenden Speicherung der Arbeit in eine Datenbank einverstanden.

Münster, 18. Mai 2015